



HAL
open science

Mitochondrial morphology and activity regulate furrow ingression and contractile ring dynamics in *Drosophila* cellularization

Sayali Chowdhary, Somya Madan, Darshika Tomer, Manos Mavrikis, Richa Rikhy

► **To cite this version:**

Sayali Chowdhary, Somya Madan, Darshika Tomer, Manos Mavrikis, Richa Rikhy. Mitochondrial morphology and activity regulate furrow ingression and contractile ring dynamics in *Drosophila* cellularization. *Molecular Biology of the Cell*, 2020, 31 (21), pp.2331-2347. 10.1091/mbc.E20-03-0177 . hal-02914318

HAL Id: hal-02914318

<https://hal.science/hal-02914318v1>

Submitted on 11 Aug 2020

HAL is a multi-disciplinary open access archive for the deposit and dissemination of scientific research documents, whether they are published or not. The documents may come from teaching and research institutions in France or abroad, or from public or private research centers.

L'archive ouverte pluridisciplinaire **HAL**, est destinée au dépôt et à la diffusion de documents scientifiques de niveau recherche, publiés ou non, émanant des établissements d'enseignement et de recherche français ou étrangers, des laboratoires publics ou privés.

Mitochondrial morphology and activity regulate furrow ingression and contractile ring dynamics in *Drosophila* cellularization

Sayali Chowdhary, Somya Madan, Darshika Tomer¹, Manos Mavrakakis² and Richa Rikhy*

Affiliation and contact information:

Biology, Indian Institute of Science Education and Research, Homi Bhabha Road, Pashan, Pune, 411008, India Phone: +91-20-25908065

1.Present address: Rutgers University, Department of Cell Biology and Molecular Medicine, 185, South Orange Avenue, Newark, NJ, USA

2.Aix Marseille Univ, CNRS, Centrale Marseille, Institut Fresnel, Marseille, France

* To whom correspondence is addressed: richa@iiserpune.ac.in

Running title: Mitochondrial shape in cellularization

Key words: mitochondrial morphology, Drp1, ROS, cellularization, *Drosophila*, embryogenesis

Abbreviations: Drp1, Dynamin related protein 1, ROS, reactive oxygen species

Abstract

Mitochondria are maternally inherited in many organisms. Mitochondrial morphology and activity regulation is essential for cell survival, differentiation and migration. An analysis of mitochondrial dynamics and function in morphogenetic events in early metazoan embryogenesis has not been carried out. In our study we find a crucial role of mitochondrial morphology regulation in cell formation in *Drosophila* embryogenesis. We find that mitochondria are small, fragmented and translocate apically on microtubules and distribute progressively along the cell length during cellularization. Embryos mutant for mitochondrial fission protein, Drp1, die in embryogenesis and show an accumulation of clustered mitochondria on the basal side in cellularization. Additionally, Drp1 mutant embryos contain lower levels of reactive oxygen species (ROS). ROS depletion has been previously shown to decrease Myosin II activity. Drp1 loss also leads to Myosin II depletion at the membrane furrow thereby resulting in decreased cell height and larger contractile ring area in cellularization similar to Myosin II mutants. The mitochondrial morphology and cellularization defects in Drp1 mutants are suppressed by reducing mitochondrial fusion and increasing cytoplasmic ROS in superoxide dismutase mutants. Our data show a key role for mitochondrial morphology and activity in supporting the morphogenetic events that drive cellularization in *Drosophila* embryos.

Highlight summary

This study shows that Drp1 regulated mitochondrial fission is essential for mitochondrial distribution across the cell in cellularization during *Drosophila* embryogenesis. Loss of mitochondrial fission in Drp1 mutant embryos leads to defects in morphogenetic events of cell formation and contractile ring constriction in cellularization.

Introduction

Organelles such as mitochondria are predominantly maternally inherited in metazoan embryos (Ukeshima and Fujimoto, 1984; Pepling and Spradling, 2001; Wilding *et al.*, 2001; Dumollard *et al.*, 2006; Zhang *et al.*, 2008). Mitochondria are semi-autonomous organelles that are involved in energy production and calcium buffering in the cell. They produce reactive oxygen species (ROS) as a by-product of the electron transport chain and important metabolites that interact with various processes in a eukaryotic cell.

Mitochondria are small and fragmented in the early blastoderm vertebrate and invertebrate embryos (Bavister and Squirrell, 2000; Sathananthan and Trounson, 2000; Van Blerkom *et al.*, 2002; Dumollard *et al.*, 2007; Chowdhary *et al.*, 2017). Mitochondrial size and shape are regulated by dedicated fission and fusion machinery. Fission protein Drp1 (Dynamin related protein 1) oligomerizes around the outer mitochondrial membrane to form smaller daughter mitochondria. Opa1 (Optic atrophy 1) and Mfn/Mfn2 (Mitofusins) (Mitochondrial assembly regulating factor; Marf in *Drosophila*) are involved in the fusion of inner and outer membrane respectively (van der Bliek *et al.*, 2013). Mitochondrial shape and cristae architecture have been correlated with their metabolic output, ROS and calcium buffering (Yu *et al.*, 2006; Hom *et al.*, 2010; Chen *et al.*, 2012; Cogliati *et al.*, 2013; Mishra and Chan, 2016; Toyama *et al.*, 2016). Loss of proteins regulating mitochondrial morphology during embryogenesis leads to abrogation of development. Drp1, Mfn and Opa1 knockout mice are embryonic lethal (Chen *et al.*, 2003; Ishihara *et al.*, 2009; Wakabayashi *et al.*, 2009; Moore *et al.*, 2010).

Mitochondrial morphology regulation is important for their efficient transport within cells. Mitochondria travel on microtubules with the help of specific motors to distinct locations in the cell (Yaffe *et al.*, 1996; Hollenbeck and Saxton, 2005; Saxton and Hollenbeck, 2012; Schwarz, 2013). Their transport to distinct locations in neurons is required for local energy supply and calcium buffering which is essential for neuronal synapse function (Morris and Hollenbeck, 1993; Mironov and Symonchuk, 2006; Rice

and Gelfand, 2006; Saotome *et al.*, 2008; Wang and Schwarz, 2009). Fused mitochondria in Drp1 mutant neurons accumulate in the cell body and axon and lead to lowered synaptic activity (Verstreken *et al.*, 2005; Rikhy *et al.*, 2007).

The literature altogether points to the involvement of mitochondrial shape and function in morphogenetic processes in metazoan embryogenesis. However, the mechanism and function of mitochondrial morphology regulation during embryogenesis remains to be studied. In this study, we aim to discern the function of mitochondrial morphology and distribution during cell formation in *Drosophila* embryogenesis. The *Drosophila* blastoderm embryo is a syncytium where nuclear cycles (NC) 1 to 13 occur in a common cytoplasm. Cell formation occurs in the prolonged interphase of NC14 in a process called cellularization. During cellularization, the short cell membranes of approximately 3-5 μm length extend basally in a synchronous manner in the entire embryo. This forms a cortical layer of approximately 6000, tall epithelial cells of 40-45 μm height in about 45-50 mins (Lecuit and Wieschaus, 2000; Mazumdar and Mazumdar, 2002). The membrane extension is accompanied by the assembly of actomyosin contractile structures at ingressing membrane fronts (Warn and Robert-Nicoud, 1990; Young *et al.*, 1991; Schejter and Wieschaus, 1993; He *et al.*, 2016) along with cytoskeletal remodelling proteins (Afshar *et al.*, 2000; Field *et al.*, 2005; Grosshans, 2005; Mavrikis *et al.*, 2014) to constrict the membrane at the base and enclose the cytoplasmic contents within the cells.

We examined whether mitochondrial morphology and distribution are regulated during *Drosophila* cellularization. Mitochondria are small, fragmented and abundant in the syncytial *Drosophila* embryos (Chowdhary *et al.*, 2017). We found that mitochondria were fragmented and enriched basally at the start of cellularization. Their distribution became pronounced apically during cellularization by microtubule based transport. The apical transport of mitochondria failed upon their clustering in mitochondrial fission protein Drp1 mutant embryos. Drp1 depletion resulted in a decrease in cytoplasmic ROS and defects in furrow ingression and contractile ring constriction, similar to Myosin II mutants. These defects were suppressed upon forced mitochondrial fission and elevation of cytoplasmic ROS in Drp1 mutant embryos. Our study proposes a role for

mitochondrial morphology and activity in maintaining a threshold of active Myosin II function to drive cell formation and contractile ring constriction during *Drosophila* embryogenesis.

Results

Mitochondria translocate apically and distribute throughout the cell during cellularization

The *Drosophila* blastoderm embryo consists of a single layer of nuclei present at the embryo cortex at the start of cellularization in the interphase of nuclear cycle 14 (Figure 1A). Myosin II is assembled at the base of the membrane furrow during this stage and reaches a peak during mid-cellularization (He *et al.*, 2016; Xue and Sokac, 2016). Myosin II aids in circularization and constriction of the membrane at the furrow tip as the furrow progresses to the basal side (Figure 1A). Mitochondria are fragmented and are distributed towards the basal regions during nuclear cycle 10-13 in the syncytial *Drosophila* embryos (Chowdhary *et al.*, 2017). In order to analyse the mitochondrial distribution along the apico-basal axis during cellularization, we imaged live embryos expressing UASp-Mito-GFP with *nanos*-Gal4 (Mito-GFP) and mCherry tagged Myosin regulatory light chain (Sqh) under the *sqh* promoter (Sqh-mCherry) upto 40 μm depth from the cortex at 25 °C (Figure 1B). We quantified the mean Mito-GFP fluorescence intensity from apical to basal sections with 1 μm increments at 3 different time points during cellularization: early (0 min), mid (~22 min) and late (~45 min) (Figure 1B,C, Movie S1). Mito-GFP fluorescence was enriched basally in the early cellularization timepoint, similar to their distribution in syncytial embryos (Chowdhary *et al.*, 2017) (Figure 1B; early, C; red). At the mid cellularization timepoint, mitochondrial fluorescence accumulated apically, showing two peaks of mitochondrial fluorescence, apically and basally (Figure 1B; mid, C; green). By the end of cellularization, mitochondrial fluorescence showed a single peak towards the apical side (Figure 1B; late, C; blue). The mitochondrial fluorescence increased in apical regions with time as also seen in sagittal sections of Mito-GFP::Sqh-mCherry embryos (Figure 1D, Movie S2). We quantified the total Mito-GFP fluorescence across 40 μm during cellularization

and found that the fluorescence did not change significantly (Figure S1A,B). This suggested that there was no significant biogenesis of mitochondria during this time period and mitochondria were likely to be enriched in apical regions due to translocation from the basal regions. The membrane ingression is known to occur in two phases: a slow phase of membrane ingression followed by a fast phase (Warn and Magrath, 1983; Merrill *et al.*, 1988; Lecuit and Wieschaus, 2000; Royou *et al.*, 2004; Figard *et al.*, 2013; He *et al.*, 2016). We measured membrane length across time during cellularization and obtained a similar trend (Figure 1E, grey). We also quantified the Mito-GFP fluorescence in the area above the furrow tips (Figure 1D, bracketed area) with respect to time. We observed an increase in Mito-GFP in the forming cells as the furrow ingressed during cellularization (Figure 1E, black).

Mitochondria and other organelles in the *Drosophila* blastoderm embryo are compartmentalized to one nucleocytoplasmic domain with very little exchange between the neighbouring syncytial cells (Frescas *et al.*, 2006; Chowdhary *et al.*, 2017). Therefore, the apical redistribution of mitochondria seen in cellularization is likely due to their transport from the basal side. We tested this possibility by photoactivating mitochondrially localized photoactivatable GFP (Mito-PAGFP) expressed using *nanos-Gal4*. We photoactivated Mito-PAGFP highlighting mitochondria below the nuclei in a region of interest (ROI) (red) at 12-15 μm from the apical surface in early cellularization stage embryos imaged sagittally (Figure 1F), and followed the fluorescent signal across successive time points during cellularization (Figure 1G). We measured the mean fluorescence intensity in apical (green) and basal (red) regions as the cellularization progressed (Figure 1H). Fluorescence rapidly moved apically (green) from the basal region (red) within 1 min after photoactivation. The fluorescence intensity kept increasing in the apical regions for 40 mins during the entire cellularization process (Figure 1G,H, Movie S3). By the end of cellularization, fluorescence was almost entirely lost from the basal regions and was enriched apically (Figure 1G,H).

We visualized mitochondrial distribution in cellularization by imaging embryo sections of early, mid and late stages using transmission electron microscopy (TEM) (Figure 1I,J). Mitochondria were seen as electron dense structures in the EM sections in

early, mid and late cellularization (Figure 1I,J). We quantified the number of visible mitochondria in apical regions above the nuclei in TEM sections and found that these numbers significantly increased in mid and late cellularization compared to the early stage (Figure 1K). Therefore we conclude that mitochondria are transported to the apical region from the basal region during cellularization and this translocation occurs coincidentally with membrane ingression.

Mitochondrial redistribution during cellularization is regulated by microtubule based transport

During cellularization, microtubules are oriented in the apico-basal axis with centrioles present above the nuclei and plus ends pointing towards the basal regions (Karr and Alberts, 1986). Microtubule based apical transport of Golgi complexes (Sisson *et al.*, 2000; Papoulas *et al.*, 2005) and basal transport of lipid droplets have been reported during late cellularization (Welte *et al.*, 1998; Arora *et al.*, 2016). Bi-directional transport of mitochondria on microtubules has been well characterized in axons (Morris and Hollenbeck, 1993). The kymograph from the photoactivation movie of Mito-PAGFP during cellularization identified linear tracks of mitochondrial transport towards the apical direction (Figure S1C, red arrowheads), suggesting that mitochondria are likely to be transported in a microtubule-based manner. To explore the link between microtubules and mitochondrial distribution, we expressed Mito-GFP and Tubulin-mCherry (Tub-mCherry) with *nanos*-Gal4 to image mitochondria and microtubules together. Microtubules were organised like an inverted basket around the nuclei and mitochondria were juxtaposed to microtubule filaments (Figure 2A). We could visualize mitochondria moving adjacent to microtubules to apical regions with time (Figure 2A, sagittal, white arrowheads, Movie S4). Mitochondria (green) and tubulin (red) showed overlapping peaks of fluorescence intensity (Figure 2A-B; white dashed line; 6 μ m).

To study the role of microtubule motors in regulating the mitochondrial distribution, we expressed RNAi to knockdown Kinesin heavy chain (*khc*¹) and Dynein heavy chain (*dhc*¹) with *nanos*-Gal4 and stained the embryos with fluorescently coupled streptavidin to mark mitochondria (Hollinshead *et al.*, 1997; Chowdhary *et al.*, 2017).

Mitochondria were predominantly present in the basal regions in the syncytial division cycles (Chowdhary *et al.*, 2017). Thus during early cellularization, few distinct and sparse mitochondria were observed at the subapical region in control embryos (Figure 2C,D). Similar to our observations in the syncytial blastoderm embryo (Chowdhary *et al.*, 2017), mitochondria were clustered sub-apically in the early cellularization stages in 100% of the *khc*^j embryos (Figure 2D, sagittal, white arrowheads), consistent with a role of kinesin in regulating plus ended movement of mitochondria in syncytial cycles and early cellularization. Mitochondria translocated apically towards the minus ends of microtubules during cellularization and their distribution was predominant in apical regions in late cellularization. The mitochondrial intensity was seen at the apical regions in sagittal sections and comparatively fewer, distinct mitochondria were observed at the basal regions near the contractile rings in surface views in control embryos (Figure 2E,F). We observed basal accumulation of mitochondria in contractile rings in late cellularization stages in 93% of the *dhc*^j embryos (Fig 2F, sagittal, white arrowheads) with few mitochondria present at the apical regions (Fig. 2F, sagittal, yellow arrowheads), suggesting that minus-end directed microtubule transport is mediating the translocation of mitochondria to the apical region.

Mitochondrial Rho GTPases (*miro*) interact with microtubule motors kinesin (Fransson *et al.*, 2006) and dynein (Morlino *et al.*, 2014), as well as adapter protein Milton (Morlino *et al.*, 2014; Melkov *et al.*, 2016) to facilitate bidirectional transport of mitochondria (Guo *et al.*, 2005; Russo *et al.*, 2009). We assessed the role of microtubule motors in the apical mitochondrial transport during cellularization using RNAi based approach to knockdown Miro (*miro*¹) using *nanos*-Gal4. In 86.4% of the *miro*¹ embryos, mitochondria accumulated in basal regions (Figure 2F; sagittal, white arrowheads) near contractile rings during early as well as late cellularization and were absent apically (Figure 2F; sagittal, yellow arrowheads). These results together showed that apical transport of mitochondria during cellularization depends on minus-end directed microtubule transport mediated by Dynein motors and Miro.

Maternal depletion of mitochondrial fission protein, Drp1 leads to embryo lethality and accumulation of clustered mitochondria basally during cellularization

Since we observed that mitochondria were small and fragmented in early *Drosophila* embryos, we assessed the distribution of mitochondrial fission protein Drp1 in cellularizing embryos. Immunostaining against Drp1 showed that it was localized to mitochondria in cellularization (Figure S2A). We depleted Drp1 maternally in two ways: we over-expressed a GTPase domain mutant of Drp1, Drp1^{SG}, and an RNAi against Drp1 (*drp1ⁱ*) with *nanos*-Gal4::UASp-Mito-GFP. When the *nanos*-Gal4 was crossed to both the Mito-GFP and each Drp1 mutant transgenes, 84% (± 7.8) Drp1^{SG} and 73% (± 14.7) *drp1ⁱ* embryos were lethal and did not hatch to produce larvae at 24 hours after laying (n = 300 each). The embryonic lethality of Drp1^{SG} and *drp1ⁱ* increased to 99% (± 1.7) and 100% respectively (n = 300) where the *nanos*-Gal4 was crossed to the Drp1 mutants alone. Thus, maternal depletion of Drp1 led to embryonic lethality.

Both Drp1^{SG} and *drp1ⁱ* embryos had clustered mitochondria in cellularization (Figure 3A). We quantified the mean area of optically resolvable fluorescent punctae of mitochondria per embryo and found that control embryos had a mean area of 0.25 (± 0.075) μm^2 . Mitochondrial fluorescence was spread over a larger area in Drp1^{SG} and *drp1ⁱ* with mean area of 0.7 (± 0.4) μm^2 and 2.2 (± 1.4) μm^2 respectively indicating clustering or elongation or fusion of mitochondria in the *Drp1* mutant embryos (Figure 3B). Mitochondrial fusion and electrical continuity has been noted on loss of Drp1 in *Drosophila* follicle cells in previous studies (Mitra *et al.*, 2012).

Mitochondrial fission is important for the translocation of mitochondria on microtubules in neurons (Chen and Chan, 2009) and Drp1 mutant neurons show an accumulation of mitochondria in the cell body and axon (Verstreken *et al.*, 2005; Rikhy *et al.*, 2007; Choi *et al.*, 2013). We assessed the basal to apical mitochondrial transport in Mito-GFP expressing Drp1^{SG} embryos during cellularization (Figure 3C). Drp1^{SG} embryos containing Mito-GFP had reduced fluorescence (Figure 3C) as compared to controls (Figure 1B) and Mito-GFP fluorescence had to be acquired at a higher laser power as compared to controls. Mitochondria in Drp1^{SG} embryos were visible more

distinctly and clearly in streptavidin stained embryos compared to Mito-GFP containing embryos, thus allowing us to quantitate their architecture (Figure 3B). However, like controls, we obtained relative Mito-GFP fluorescence intensity estimates within each $Drp1^{SG}$ expressing living embryo to analyse mitochondrial localization during cellularization and furrow extension. The relative mean mitochondrial fluorescence was obtained at 3 time points: early, mid and late cellularization, along the apico-basal axis with 1 μm depth increments for total 30 μm depth. Similar to the control embryos (Figure 1B), the Mito-GFP intensity was basally pronounced in the early cellularization (Figure 3C; top panel, 3D; red). However unlike controls, the apical regions in $Drp1^{SG}$ did not gain fluorescence at the following time points at mid (Figure 3C; middle panel, 3D; green) cellularization. At late cellularization there was a mild increase in the apical intensity but the peak of mitochondrial intensity remained in basal regions (Figure 3C, bottom panel, 3D; blue). Similar to $Drp1^{SG}$, $drp1^i$ embryos also showed lack of change in the Mito-GFP signal distribution from basal to apical from early to mid and late stages during cellularization (Figure S2B). The mean mitochondrial fluorescence intensity remained at a peak in basal regions in these embryos during cellularization (Figure S2C).

We further measured the total mitochondrial fluorescence incorporated within the forming cells above the furrow tip as the furrow extended basally. The membrane extension took place in the slow and fast phase in $Drp1^{SG}$ mutant embryos similar to controls (Figure 1E). However, unlike the control embryos, mitochondrial fluorescence did not show an increase with time, remaining lower than controls (Figure 3E). Mitochondrial fluorescence intensity remained higher below the furrow (marked with Sqh-mCherry) in $drp1$ mutant embryos and did not get effectively incorporated in the forming cell likely due to lack of their transport (Figure 3C).

We confirmed the decreased apical transport in $Drp1^{SG}$ embryos by photoactivation using Mito-PAGFP. We photoactivated fluorescence in early cellularization embryos in a region below the nuclei (Figure 3F, red) and followed the fluorescence in the apical region (Figure 3F, green) as depicted. The photoactivated mitochondrial fluorescence in basal regions of $Drp1^{SG}$ embryos remained basal and was

not transported to the apical region (Figure 3G, Movie S5). We quantified mean fluorescence intensity in the basal (red) and apical (green) regions. There was no significant depletion in the fluorescence intensity signal of the basal region, and the apical region did not gain any fluorescence either, further demonstrating the lack of apical transport of mitochondria (Figure 3H). Our data together show that the loss of mitochondrial fission by Drp1 depletion leads to larger mitochondria which do not translocate apically and accumulate at the basal regions during cellularization.

In an attempt to decrease mitochondrial clustering in Drp1^{SG} embryos, we expressed RNAi against mitochondrial fusion protein Opa1 (*opa1ⁱ*) in Drp1^{SG} embryos (Drp1^{SG}; *opa1ⁱ*). Flies expressing *opa1ⁱ* alone did not lay embryos, however, flies expressing Drp1^{SG}; *opa1ⁱ* combination gave embryos which were lethal (87.5% unhatched, n = 180 embryos). We measured the mean area of optically separable fluorescent mitochondrial structures per embryo in apical (Fig. S3A, apical, 3 μm depth) and basal sections (Fig. S3A, basal, depth ≥ 15 μm) near the contractile rings (Fig. S3A) in streptavidin stained control, Drp1^{SG} and Drp1^{SG}; *opa1ⁱ* embryos. The area of apical mitochondrial fluorescent punctae was similar in all the combinations (Figure S3A, B; apical). There was no significant difference between apical and basal mitochondrial sizes in controls (Figure S3B). The mitochondrial punctae at the basal region in Drp1^{SG} were much larger at an average of $0.9 (\pm 0.5) \mu\text{m}^2$ in size, compared to the control mitochondria that were $0.3 (\pm 0.2) \mu\text{m}^2$ in size (Figure S3B, red, black respectively). The basal mitochondrial size defect seen in Drp1^{SG} embryos was completely suppressed in Drp1^{SG}; *opa1ⁱ* ($0.34, \pm 0.05 \mu\text{m}^2$) embryos (Figure S3B).

We further quantified the apical density of mitochondria in late cellularization stage embryos as a measure of mitochondrial apical translocation during cellularization. For this we quantified the relative mitochondrial area occupied in apical regions above the nucleus in mid-late cellularization stage embryos with furrow length above 12 μm . On average, mitochondria occupied $7.2 (\pm 2.8) \%$ of the apical area in control embryos (Figure S3C, black). The mean relative area decreased to $0.3 (\pm 0.4) \%$ in Drp1^{SG} (Figure S3C, red) embryos and was consistent with the analysis of mitochondrial distribution done using Mito-GFP (Figure 3C, D) and Mito-PA-GFP (Figure 3G, H)

embryos that showed presence of mitochondrial clusters at the basal region and lack of apical translocation. Compared to Drp1^{SG}, the relative mean mitochondrial area increased to about 6.1 (± 2.2) % in Drp1^{SG};opa1ⁱ embryos (Figure S3C, blue). Thus, increase in mitochondrial size led to basal accumulation of mitochondria in Drp1^{SG} embryos and this phenotype was suppressed in Drp1^{SG};opa1ⁱ embryos.

Together these data show that maintenance of mitochondrial fission is essential for their translocation to apical locations during cellularization.

Drp1 depletion leads to decrease in cytoplasmic reactive oxygen species

Mitochondrial shape changes lead to alterations in their metabolic activity and ATP production (Mishra and Chan, 2016). Decrease in ATP production leads to accumulation of AMP which triggers phosphorylation of AMPK (pAMPK) (Sakamoto *et al.*, 2005; Hardie and Sakamoto, 2006). Mitochondria are the major source of ATP in *Drosophila* blastoderm embryos (An *et al.*, 2014; Chowdhary *et al.*, 2017). Mutations in electron transport chain components lead to decrease in ATP and elevation of pAMPK. Electron transport chain mutant embryos showed a reduction in the metaphase furrow lengths in the syncytial *Drosophila* embryos (Chowdhary *et al.*, 2017). We tested for ATP stress response in Drp1^{SG} embryos using pAMPK staining. Both control and Drp1^{SG} embryos were imaged using identical laser settings. During cellularization, pAMPK showed a cytoplasmic distribution with enrichment in punctae in the apical region. (Figure 4A). The quantification of mean pAMPK intensity in apical sections in Drp1^{SG} did not show a significant difference as compared to the controls indicating that the embryos did not have increased AMP, and ATP stress (Figure 4B).

ROS is produced as a byproduct of the electron transport chain activity (Liu *et al.*, 2002; Bell *et al.*, 2007). ROS has been implicated in the regulation of differentiation and morphogenetic movements in embryos (Ji *et al.*, 2010; Muliylil and Narasimha, 2014; Hunter *et al.*, 2018). We assessed ROS levels in the cytoplasm using fluorescent dihydroethidium (DHE) staining in control and Drp1^{SG} embryos (Figure 4C). DHE oxidation due to the presence of ROS leads to its fluorescence at 561 nm, thus providing a quantitative readout for the amount of ROS in cells, and allowing the

comparison of different genotypes when imaged with the same laser settings (Figure 4C, D). Drp1^{SG} embryos showed significantly lowered mean fluorescence compared to controls (Figure 4C,D). These data are in agreement with other studies that show reduction of ROS in fission mutants (Yu *et al.*, 2006; Röth *et al.*, 2014; Son *et al.*, 2015; Kim *et al.*, 2018). We overexpressed mutant human superoxide dismutase 1 (hSOD1^{A4V}) as a positive control to test for increased ROS in embryos. hSOD1^{A4V} expression does not have any SOD activity (Watson *et al.*, 2008; Islam *et al.*, 2012). We observed ~3 fold increase in the mean cytoplasmic DHE fluorescence in hSOD1^{A4V} expressing embryos as compared to controls (Figure 4C,D). Thus, Drp1^{SG} embryos containing clustered mitochondria have decreased ROS without any ATP stress.

Drp1 depletion leads to defects in contractile ring constriction and membrane extension in cellularization

ROS levels are important for regulating Myosin II based apical constriction of epithelial cells in dorsal closure and wound healing (Mulyil and Narasimha, 2014; Hunter *et al.*, 2018). Since mitochondria were clustered and ROS was decreased in Drp1^{SG} embryos, we analysed the distribution and function of Myosin II during cellularization. During cellularization, the furrow ingresses basally, along with an assembly of an actomyosin ring at the furrow tip followed by ring constriction (Figure 1A). We imaged *sqh*-Sqh-mCherry (Sqh-mCherry) embryos in the sagittal orientation for visualising the furrow ingression with time from the start of cellularization until gastrulation at the same laser power and gain settings (Figure 5A, Movie S6). We measured furrow membrane length by Sqh-mCherry enrichment at furrow tips every 2 mins in control (black) and Drp1^{SG} (red) embryos (Figure 5B) as it ingressed basally during cellularization. Both genotypes exhibited similar ingression kinetics with an initial slow phase upto 20 mins, followed by a fast phase until the completion of cellularization (Figure 5A,B). This ingression trend has been reported before in cellularization (Merrill *et al.*, 1988; Lecuit and Wieschaus, 2000; Figard *et al.*, 2013; He *et al.*, 2016; Xue and Sokac, 2016) leading to the formation of columnar epithelial cells of approximately 40 μm height. The membrane ingression process stopped and Sqh-mCherry signal reduced from furrow tips at approximately 40 mins in Drp1^{SG} embryos (Figure 5A;

arrowhead, 5B; red, Movie S7) and resulted in significantly shorter cells at an average height of $29.3 (\pm 1.3) \mu\text{m}$ (Figure 5B; red, C) compared to $40.8 (\pm 1.9) \mu\text{m}$ in controls (Figure 5B; black, C).

We imaged Sqh-mCherry control and Drp1^{SG} mutant embryos in 3 dimensions over time to analyse the Sqh levels and the area of rings to estimate constriction at the furrow tip in cellularization with the same laser power and gain settings. Cross sectional images of the growing furrow tips allowed us to monitor both Sqh-mCherry localization and membrane architecture at the tips as the furrow grows deeper with time (Figure 5D). The base of the furrow was polygonal at the start of cellularization (Figure 5D; $5 \mu\text{m}$). During the slow to fast phase transition, the membrane organization changed from polygonal to circular. During the fast phase, rings constricted rapidly (Figure 5D, $12 \mu\text{m}$ onwards). We measured the mean Sqh-mCherry intensity at the furrow tips with respect to the length of membrane furrow in control and Drp1^{SG} embryos. Control embryos showed an initial increase in the Sqh-mCherry intensity until approximately $15 \mu\text{m}$ of furrow length after which the signal gradually dropped (Figure 5E; black). Drp1^{SG} embryos showed an overall decrease in Sqh-mCherry intensity at the membrane front (Figure 5E; red). Constriction was calculated by measuring the contractile ring area with respect to the length in cellularizing embryos (Figure 5F). The area of contractile rings in Drp1^{SG} (Figure 5F; red) was similar to control embryos (Figure 5F; black) at the beginning of cellularization, but it remained larger compared to controls (Figure 5F). The area of contractile rings at the end of cellularization was significantly larger in Drp1^{SG} embryos ($19, \pm 4.3 \mu\text{m}^2$) compared to controls ($10.2, \pm 1.1 \mu\text{m}^2$) (Figure 5G).

Since mitochondrial morphology and apical transport defects seen in Drp1^{SG} were suppressed on inhibiting mitochondrial fusion in Drp1^{SG}; *opa1*ⁱ, we asked whether the decrease in cell height and contractile ring defect observed in Drp1^{SG} embryos could also be suppressed on additional depletion of Opa1. To analyse membrane ingression dynamics, we imaged sagittal sections of Drp1^{SG}; *opa1*ⁱ embryos using *sqh*-Sqh-GFP (Sqh-GFP) (Figure S4A, Movie S8). The relative fluorescence levels in Sqh-GFP and Sqh-mCherry embryos were comparable across cellularization (Figure S5). Membrane length was estimated with Sqh-GFP localized at the furrow tips (Figure

S4A,B). Furrow ingression rates in $Drp1^{SG}$; $opa1^i$ (blue) embryos were similar to controls (black) (Figure S4B). The membranes reached $36 (\pm 2.3) \mu\text{m}$ in $Drp1^{SG}$; $opa1^i$ embryos (Figure S4C, blue), and this was significantly more compared to $Drp1^{SG}$ embryos (Figure S4C, red, Movie S8).

We measured Sqh intensity in the contractile rings in $Drp1^{SG}$; $opa1^i$ embryos and compared it to Sqh-GFP controls (Figure S4D,E). The Sqh-GFP intensity in $Drp1^{SG}$; $opa1^i$ embryos (Figure S4E, blue) increased as compared to $Drp1^{SG}$ embryos (Figure S4E, red) but was lower than controls (Figure S4E, black). The area of contractile rings in $Drp1^{SG}$; $opa1^i$ (Figure S4F, blue) embryos decreased faster compared to $Drp1^{SG}$ alone (Figure 5F, S4F, red), with the area being comparable to control embryos at $35 \mu\text{m}$ membrane length (Figure S4F, black). The contractile ring area, measured at the end of cellularization in $Drp1^{SG}$; $opa1^i$ embryos ($12.6, \pm 5 \mu\text{m}^2$), was smaller than $Drp1^{SG}$ (Figure S4G).

We over-expressed a non-phosphorylatable version of *sqh* (pUASp-Sqh^{A20A21}, Sqh^{AA}) (Vasquez *et al.*, 2014) with *nanos*-Gal4 to analyse the effects of Myosin II inactivation on the furrow extension and ring shape dynamics (Figure 5A). Previous studies show that Sqh^{AA}, when expressed in the background of the hypomorphic *sqh*¹ allele, leads to loss of contractility in cellularization (Xue and Sokac, 2016). Sqh^{AA} has also been shown to localize to sites of actomyosin function and cause loss of actomyosin contractility in a dominant negative manner when expressed in the wild type background (Jordan and Karess, 1997; Sen *et al.*, 2012; Zhang *et al.*, 2018; Das Gupta and Narasimha, 2019; Mishra *et al.*, 2019). Furrow extension in Sqh^{AA} embryos occurred in a slow and fast phase similar to control and $Drp1^{SG}$ embryos (Figure 5A,B). Uneven furrow extension in the fast phase has been shown previously for *sqh*¹ (Royou *et al.*, 2004) and *sqh*¹;*sqh*^{AA} combination (Vasquez *et al.*, 2014). We observed shorter cells at an average length of $28.2 (\pm 4.6) \mu\text{m}$ in Sqh^{AA} expressing embryos (Figure 5A-C; light red, Movie S9). Reduced constriction of the contractile ring has been observed in embryos with lowered Myosin II activity previously (Wenzl *et al.*, 2010; Mavrakis *et al.*, 2014; He *et al.*, 2016; Xue and Sokac, 2016). Expectedly, Sqh^{AA} embryos had lowered Sqh-mCherry at the furrow tips during cellularization (Figure 5A, D, E; light red)

and decreased ring constriction (Figure 5F; light red) with a significantly larger contractile ring area $25.1(\pm 9.1) \mu\text{m}^2$ at the end of cellularization (Figure 5G; light red).

These data together show that shorter cell height and impaired actomyosin constriction in Drp1^{SG} embryos occurs due to reduced Myosin II function.

Increasing ROS suppresses mitochondrial clustering defects in Drp1 mutant embryos

ROS has been previously shown to regulate mitochondrial fragmentation in cells undergoing dorsal closure in *Drosophila* embryogenesis (Mulyil and Narasimha, 2014). We, therefore, assessed the mitochondrial morphology and distribution in hSOD1^{A4V} and Drp1^{SG};hSOD1^{A4V} expressing embryos. Mitochondria were depleted in apical regions (Figure 6A, apical) and accumulated in basal regions in Drp1^{SG} embryos (Figure 6A, basal and sagittal white arrowheads) as compared to controls. The mitochondrial organization in apical and basal regions was similar to controls in hSOD1^{A4V} embryos. This loss in apical mitochondria in Drp1^{SG} was suppressed in Drp1^{SG};hSOD1^{A4V} (Figure 6A, apical and sagittal, yellow arrowheads). We measured the mean area of optically separable fluorescently labelled mitochondrial structures in apical sections at 3 μm depth from the cortex and basal sections near the contractile rings in control, Drp1^{SG}, hSOD1^{A4V} and Drp1^{SG};hSOD1^{A4V} mid to late cellularization stage embryos. The mean area of mitochondria in apical and basal regions in hSOD1^{A4V} (basal - $0.16 \pm 0.12 \mu\text{m}^2$) (Figure 6B; green) and Drp1^{SG};hSOD1^{A4V} (basal - $0.3 \pm 0.19 \mu\text{m}^2$) (Figure 6B; blue) embryos was comparable to controls (Figure 6B; black) and significantly smaller than Drp1^{SG} (Figure 6B; red).

We also quantified the relative apical mitochondrial area to estimate apical translocation of mitochondria. The area occupied by mitochondria apically in hSOD1^{A4V} (Figure 6C; green) and Drp1^{SG};hSOD1^{A4V} (Figure 6C; blue) was, $7.4 (\pm 3.4) \%$ and $5.9 (\pm 2.1) \%$ respectively, which was comparable to controls (Figure 6C, black) and significantly more than Drp1^{SG} (Figure 6C; red). These data suggest that an increase in ROS leads to a change in mitochondrial morphology in Drp1 depleted embryos, thereby reversing the mitochondrial distribution defect in the apical and basal regions.

Contractile ring constriction and membrane ingression defects of Drp1^{SG} embryos are suppressed in Drp1^{SG};hSOD1^{A4V} embryos

Increase in phosphorylation of Myosin II subunits by Src kinases enhances their recruitment and activity at the contractile ring (Thomas and Wieschaus, 2004; Strong and Thomas, 2011). Also, Src kinase activity increases due to oxidation by elevated mitochondrial ROS during wound healing (Hunter *et al.*, 2018). Since ROS levels were reduced in Drp1^{SG} with a decrease in the Myosin II function, we analysed the furrow ingression and contractile ring dynamics in hSOD1^{A4V} and Drp1^{SG}; hSOD1^{A4V} embryos in order to test the possible role of ROS in regulating Myosin II during cellularization.

First, we analysed the membrane ingression in hSOD1^{A4V} and Drp1^{SG}; hSOD1^{A4V} embryos during cellularization (Figure 7A). Interestingly, the slow phase became shorter and the fast phase started earlier at around 16 mins in (Figure 7B; light green dotted line) hSOD1^{A4V} embryos in contrast to 20 mins in controls (Figure 7B; yellow dotted line) (Movie S10). The membrane ingression also occurred faster in hSOD1^{A4V} embryos (Figure 7B; green, Movie S10) compared to controls (Figure 5B, 7B; black, Movie S6). Drp1^{SG};hSOD1^{A4V} embryos also (Figure 7B; blue, Movie S11) showed faster ingression as compared to controls (Figure 5B, 7B; black, Movie S6) during the fast phase. The average length of cells at the end of cellularization in hSOD1^{A4V} embryos (44.7, ± 3.3 µm) was longer than controls (Figure 7C; green), whereas the length in Drp1^{SG}; hSOD1^{A4V} (Figure 7C; blue) embryos (38.6, ± 3.7 µm) was similar to controls thus suppressing the membrane ingression defects of Drp1^{SG} embryos (Figure 7C; red, Movie S11).

We quantified Sqh fluorescence levels and ring constriction dynamics in hSOD1^{A4V} and Drp1^{SG}; hSOD1^{A4V} embryos. These were imaged at the same laser power and gain setting as the respective control embryos. Sqh-mCherry fluorescence intensity at contractile rings in hSOD1^{A4V} alone (Figure 7D, E; green) was elevated compared to Sqh-mCherry controls (Figure 5D,5E, 7D,7E; black). Sqh-GFP intensity in Drp1^{SG}; hSOD1^{A4V} embryos (Figure 7E; blue) was similar to Sqh-GFP controls (Figure 7E; black). Ring constriction in hSOD1^{A4V} (Figure 7F; green) occurred faster compared

to controls (Figure 5F, 7F; black) and ring area achieved at the end of cellularization ($6.6 \pm 1.97 \mu\text{m}^2$) was significantly lower compared to the control embryos (Figure 7G; green, black respectively). The decrease in contractile ring area with respect to membrane length in Drp1^{SG}; hSOD1^{A4V} embryos (Figure 7F; blue) was similar to control embryos (Figure 5F, 7F; black) and the final ring area ($9.4 \pm 1.9 \mu\text{m}^2$) was also comparable to controls (Figure 7G; black). Thus, contractile ring constriction and membrane ingression defects of Drp1^{SG} embryos were suppressed by supplementing ROS in the Drp1^{SG}; hSOD1^{A4V} combination.

Discussion

Our study shows that mitochondria need to be fragmented in order to distribute uniformly along the apico-basal axis, thereby enabling appropriate furrow ingression and ring constriction in *Drosophila* cellularization (Figure 8). We find that the basal to apical translocation of larger, clustered mitochondria is inhibited in Drp1 mutant embryos giving rise to defects in membrane ingression and ring constriction. Given the similarity in the ring constriction and membrane ingression defects between Drp1^{SG} and Sqh^{AA} mutants and significantly lower levels of Sqh in Drp1^{SG} mutants, the defects are likely to be due to inhibition of Myosin II during cellularization (Figure 8). The suppression of these defects by supplementing ROS indicates that ROS depletion in Drp1 mutants is a likely mechanism for regulation of Myosin II activity. We discuss the implications of our findings on the following: 1) the regulation of microtubule motor activity and distribution of organelles during cellularization, 2) the role of mitochondrial size in distribution of mitochondria in distinct parts of the developing embryo and 3) the role of ROS levels in maintaining a threshold of active Myosin II for morphogenetic processes in cellularization.

Previous studies have shown that Golgi complexes associate with dynein with the help of adapter protein, Lava Lamp, and migrate apically during the late stages of cellularization (Sisson *et al.*, 2000; Papoulas *et al.*, 2005). Inhibition of Golgi activity leads to disruption of membrane extension during cellularization (Sisson *et al.*, 2000). On the other hand, lipid droplets are transported to the basal regions by kinesin (Arora

et al., 2016). Our previous analysis of depleting the plus end motor, kinesin, during syncytial division cycles of *Drosophila* embryos showed inhibition of mitochondrial transport to microtubule plus ends leading to their accumulation in apical planes (Chowdhary *et al.*, 2017). Kinesin knockdown showed premature apical accumulation of mitochondria during early cellularization. This is similar to previous analyses with lipid droplets that accumulate apically in the absence of Kinesin motors (Shubeita *et al.*, 2008). Mitochondria can bind to both dynein and kinesin adapters with the help of Miro (Saotome *et al.*, 2008; Russo *et al.*, 2009). The increased mitochondrial accumulation in basal sections in *dhcⁱ* and *miroⁱ* suggests their role in microtubule motor based apical transport of mitochondria during cellularization. Our findings and previous work on apical transport of Golgi complexes, and basal transport of lipid droplets (Welte *et al.*, 1998; Sisson *et al.*, 2000; Papoulas *et al.*, 2005) suggest a significant regulation of microtubule motors and their activity during *Drosophila* cellularization.

Mitochondrial fusion and fission proteins are maternally dumped in significant quantities in the early *Drosophila* embryo. Mitochondrial shape changed to a more clustered and fused form upon maternally depleting Drp1. The mitochondrial morphology regulation is essential for their transport in cells (Li *et al.*, 2004; Verstreken *et al.*, 2005; Chen and Chan, 2009; Saxton and Hollenbeck, 2012). On the other hand, microtubule motor activity has been recently found to be important for maintaining mitochondrial shape by allowing increased mitochondrial contact to facilitate fusion (Mehta *et al.*, 2019). Loss of mitochondrial transport to distinct locations of cells has been implicated in neurodegeneration (Costa *et al.*, 2010; Wang *et al.*, 2011; Rawson *et al.*, 2014). Drp1^{SG} embryos containing clustered mitochondria showed lack of apical mitochondrial transport which would most likely be due to inefficiency of microtubule motors in carrying elongated mitochondria. Forced fission of mitochondria by additional depletion of Opa1 in Drp1^{SG} embryos suppressed mitochondrial clustering and allowed their apical transport. This indicates that mitochondrial fission is sufficient for their apical translocation. Not surprisingly, a small number of fragmented mitochondria present in Drp1^{SG} embryos were able to translocate to apical sections.

ROS induced oxidation of kinases has been demonstrated in *in vitro* studies (Fedorova *et al.*, 2009; Steinberg, 2013). Elevated ROS levels due to hypoxia in bovine brain endothelial cells increase phosphorylation of Myosin II light chain (Kuhlmann *et al.*, 2007). Regulation of Myosin II by redox has also been demonstrated during integrin engagement (Fiaschi *et al.*, 2012). Tuning of Myosin II activity by regulation of Rho Kinase (ROCK) and Src kinase by ROS levels has been studied in *Drosophila* embryo dorsal closure and Zebrafish wound healing (Mulyil and Narasimha, 2014; Hunter *et al.*, 2018). Consistent with these studies, Drp1^{SG} embryos containing reduced ROS levels displayed a decrease in Sqh intensity leading to impaired constriction of contractile rings and shorter membrane length during cellularization. Interestingly, Drp1^{SG}; *opa1*ⁱ combination containing intermediate Sqh levels showed partial suppression of both furrow length and ring phenotypes seen in Drp1^{SG} embryos. We were able to suppress the Drp1^{SG} phenotypes by supplementing ROS by using hSOD1^{A4V}. It is likely that ROS levels are increased in Drp1^{SG}; *opa1*ⁱ embryos upon mitochondrial fragmentation, thereby suppressing the contractility and cell elongation defects in Drp1^{SG}. Similar to Drp1^{SG}, Myosin II light chain mutant, Sqh^{AA} expressing embryos also contained short furrows with less contractile rings. ROCK increases Myosin II activity by phosphorylating Sqh and inhibiting Myosin II phosphatase (MBS) (Kimura *et al.*, 1996). Inhibition of Rok affects Myosin II recruitment (Royou *et al.*, 2002; Xue and Sokac, 2016) and results in shortening of furrow length during cellularization (Royou *et al.*, 2002, 2004). On the other hand, optogenetic activation of Rho-GEF2 at the basal membrane increases Myosin II levels leading to increased ring constriction (Krueger *et al.*, 2018). Notably, hSOD1^{A4V} embryos with increased Myosin II levels had more constricted rings and longer cells compared to the control embryos. It is likely that ROS is essential for the activity of kinases such as Src and ROCK to regulate Myosin II during cellularization. Thus, the suppression of furrow ingression and ring constriction defects by increasing ROS in Drp1 mutant embryos suggests that mitochondrial morphology and ROS levels are developmentally regulated so as to maintain balanced Myosin-II activity in morphogenetic processes.

Increasing ROS in Drp1 mutant embryos suppressed mitochondrial morphology defects. Mitochondrial shape did not change in hSOD1^{A4V} embryos, possibly since

mitochondria are already fragmented. ROS has been shown to cause mitochondrial fragmentation in cells involved in dorsal closure in *Drosophila* embryos (Mulyil and Narasimha, 2014). It is possible that ROS, in order to fragment mitochondria, can reduce the activity of mitochondrial fusion proteins such as Opa1 and Marf by oxidising them directly or indirectly (Tsushima *et al.*, 2018), when Drp1 itself is inactive in mutants like Drp1^{SG}. We have previously shown that depletion of Marf in addition to Drp1 mutation leads to reversal of Drp1 defects in *Drosophila* follicle cell differentiation by reducing mitochondrial fusion (Mitra *et al.*, 2012). Our results show that depletion of Opa1 in combination with Drp1^{SG} suppresses the clustered mitochondrial morphology phenotype in *Drosophila* embryos. Thus, ROS mediated inhibition of mitochondrial fusion in Drp1^{SG} embryos may be the cause of mitochondrial fragmentation in the Drp1^{SG}; hSOD1^{A4V} embryos. Future experiments that focus on understanding how ROS can lead to mitochondrial fragmentation will provide insights into the regulation of mitochondrial shape by ROS.

In summary, we show that mitochondrial architecture, distribution, dynamics and ROS generation activity play a crucial role in morphogenetic processes involved in cell formation during *Drosophila* embryogenesis. Our study motivates an analysis of how distinct mitochondrial functions of ATP and ROS generation, regulation of metabolites and calcium buffering can regulate key morphogenetic processes in metazoan embryogenesis.

Methods

Fly stocks

All *Drosophila* crosses were maintained at 28 °C in standard cornmeal agar medium. *nanos*-Gal4 was used for inducing expression of all transgenes and RNAi. Tub-mCherry (P{UAS-ChRFP-Tub}2, Bloomington No. 25774), *khc*ⁱ (*y*¹ *sc*^{*} *v*¹ *sev*²¹; P{TRiP.HMS01519}attP2, Bloomington No.: 35770), *dhc*ⁱ (*y*¹ *sc*^{*} *v*¹ *sev*²¹; P{TRiP.GL00543}attP40, Bloomington No. 36583) *miro*ⁱ (*y*¹ *sc*^{*} *v*¹ *sev*²¹; P{TRiP.GL01583}attP2, Bloomington No.: 43973), *drp1*ⁱ (*y*¹ *v*¹; P{TRiP.HMC03230}attP40, Bloomington No. 51483), *opa1*ⁱ (*y*¹ *sc*^{*} *v*¹ *sev*²¹; P{TRiP.HMS00349}attP2, Bloomington No. 32358), UAS-hSOD1^{A4V} (*w*¹¹¹⁸; P{UAS-hSOD1.A4V}9.1/TM6B, Tb¹, Bloomington No. 33607), UASp-Sqh^{AA} (*w*^{*}; P{UASp-sqh.A20A21}3, Bloomington No. 64114), *sqh*-Sqh-mCherry (*w*^{*}; P{sqh-mCherry.M}3, 59024) and *sqh*-Sqh-GFP (*w*¹¹¹⁸; P{sqh-GFP.RLC}3, 57145) were obtained from Bloomington stock center, Indiana, USA. UASp-Drp1^{SG} and UASp-Mito-PAGFP (Chowdhary *et al.*, 2017) were generated in the RR lab. UASp-Mito-GFP was obtained from Rachel Cox. Recombinant fly stocks, *nanos*-Gal4::UASp-MitoGFP (Mito-GFP) and *nanos*-Gal4::UASp-MitoGFP::*sqh*-Sqh-mCherry (Mito-GFP::*sqh*-mCherry) were made using standard genetic crosses and were crossed with *drp1*ⁱ, Drp1^{SG}, Sqh^{AA} and hSOD1^{A4V}. Drp1^{SG};hSOD1^{A4V} and Drp1^{SG}; *opa1*ⁱ were crossed with either *nanos*-Gal4 or *sqh*-Sqh-GFP; *nanos*-Gal4. *khc*ⁱ, *dhc*ⁱ and *miro*ⁱ were crossed with *nanos*-Gal4. Embryos were obtained from F1 generation flies.

Maintaining comparable Gal4 levels across genotypes

Care was taken to maintain comparable copies of transgenes across genotypes to enable comparative expression. The *nanos*-Gal4; UASp-Mito-GFP and *nanos*-Gal4::UASp-MitoGFP::*sqh*-Sqh-mCherry recombinant line was used for expressing single mutant transgenes of *drp1*ⁱ, Drp1^{SG}, Sqh^{AA}, hSOD1^{A4V}. Double mutants Drp1^{SG};hSOD1^{A4V} and Drp1^{SG}; *opa1*ⁱ were crossed to *nanos*-Gal4 or *nanos*-Gal4;Sqh-GFP to compensate for the Gal4 amounts compared to the single mutant transgenes.

Cloning of Drp1^{SG} mutants

The conserved residue in the GTPase domain of Drp1, Serine 193 was mutated to Glycine. Primers: 5' GAC ATG GCC ACC GGC GAG GCA CTC AAG Tm= 68, Length= 27 and 5' CTT GAG TGC CTC GCC GGT GGC CAT GTC Tm= 68, Length= 27 containing flanking restriction enzyme site sequences against Drp1 with a mutation at 193rd Serine to mutate it to Glycine. Mutated sites are underlined in the primer. Flanking primers at the N and C terminus of the coding region were used to extract the sequence from the vector pOTB7 and treated with Dpn1 to get rid of the methylated strand. We further transformed the mutated vector in DH5 α cells and the colonies obtained were sent for sequencing to allow correct identification of point mutation. Correct sequences with the point mutation were further cloned into the pUASp vector and sent for injections to fly facility in NCBS, Bangalore, India.

Transmission Electron Microscopy of embryos

yw embryos were collected for 30 min at 25°C and aged for different times at 25°C to enrich in early, mid and late cellularization stages. Embryos were dechorionated with bleach, rinsed with water and fixed for 10 min in a mix of 1 mL glutaraldehyde 25% and 4 mL heptane. The heptane and glutaraldehyde phases were removed and embryos were dispersed in PBS containing 0.1% Tween20 and 0.1% BSA. Embryos were hand-devitellinized on double-stick tape with a hypodermic needle (BD Microlance 3 - 30Gx1/2", BD 304000), and embryos of the desired stages were transferred to freshly prepared fixative solution (2.5% glutaraldehyde in 50 mM cacodylate buffer pH 7.2-7.4, 0.1% tannic acid), then stored at 4°C in the same solution overnight. Embryos were post-fixed for 2 hr in 1% osmium, 2% glutaraldehyde in 50 mM cacodylate buffer at 4°C. Embryos were washed in cacodylate buffer, dehydrated in a graded ethanol series, and finally embedded in epon. 80-nm ultrathin sagittal sections were prepared with an ultramicrotome, mounted onto copper grids, contrasted with 1% uranyl acetate and examined with a FEI Tecnai G2 200 kV electron microscope. Images were acquired with a FEI Eagle CCD camera (4096x4096 pixels) for 1700x magnifications and an Olympus Veleta CCD camera (2048x2048 pixels) for 3100x and 8500x magnifications.

For a given sagittal section and stage, the acquired images covered the whole region from the apical cortex down to yolk spheres.

Live Imaging

2 hr old *nanos-Gal4::UASp-Mito-GFP*, *nanos-Gal4::UASp-Mito-GFP::sqh-Sqh-mCherry* or *sqh-Sqh-GFP;nanos-Gal4* containing embryos were collected from F1 generation flies maintained in embryo collection cages at 28 °C containing yeast supplemented sucrose-agar medium. Embryos were dechorionated using 100% bleach for 1 min and washed. They were mounted in 2 chambered cover glass dishes (LabTek, Germany) in PBS and imaged live at 25°C in a temperature controlled microscope chamber using 63x/1.4 NA objective on confocal laser scanning microscope (Zeiss LSM 710/780 or Leica SP8). Z stacks with 1 µm intervals were acquired across 50 µm from apical to basal regions. Sagittal imaging was done at embryonic sections where nuclei were visibly aligned. Care was taken to maintain the imaging within the 0-255 range on an 8-Bit scale to avoid saturation and enable image analysis.

Photoactivation

Embryos expressing Mito-PAGFP were photoactivated at rectangular regions of interest (ROIs) of 10 – 15 µm² area in basal regions (below the nuclei) in sagittal sections in early cellularization stage using 405 nm laser at 100% power and 30 iterations using 63x/1.4 NA objective on confocal laser scanning microscope (Zeiss LSM 780). Images were obtained using 488 nm excitation wavelength. Mean fluorescence intensities in photoactivated ROIs and reference ROIs were measured using ImageJ. They were normalized with the mean intensity of the photoactivated ROI at the first time point. The averaged normalized intensity values for multiple embryos were plotted with standard error of the mean (SEM) using Graphpad Prism 5.0 (Figure 1G,1H, 3G, 3H).

Immunostaining

3.5 - 4hr old embryos were obtained from collection cages, washed, dechorionated with bleach for 1 min, fixed using 1:1 heptane and 4% paraformaldehyde (PFA) in phosphate buffered saline (PBS - 137 mM NaCl, 2.7 mM KCl, 10 mM Na₂HPO₄ and 1.8 mM

KH₂PO₄) for 20 mins and devitellinized by shaking in 1:1 Heptate: Methanol or hand devitellinized using insulin needles. Hand-devitellinization was used for staining with the F-actin label, phalloidin. The embryos were then washed thrice with PBS-T (Triton X-100, 0.3%), blocked for 1 hr using 2% bovine serum albumin (BSA) and incubated with anti-pAMPK(Cell Signalling, Rabbit, 1:200) or anti-Drp1 (Leo Pallanck, Rabbit, 1:500) diluted in BSA overnight at 4°C. Fluorescently labelled secondary antibody (Molecular Probes, 1:1000) and/or fluorescently labelled streptavidin (Molecular Probes, 1:1000) and phalloidin (Molecular Probes, 1:1000) diluted in PBST were added and incubated in dark conditions at room temperature for 45 mins, followed by 3 washes with PBST. Nuclear stain Hoechst 33342 (Molecular Probes, 1:1000) was added in the second wash. The embryos were mounted on slides using Slowfade Gold (Life Technologies) and stored at 4°C. The samples were imaged using Plan Apochromat 63x/1.4 NA, oil immersion objective on confocal laser scanning microscope (Zeiss, LSM 710 or 780 or Leica SP8). Streptavidin is used as a mitochondrial marker since it probes biotinylated proteins enriched in them (Hollinshead *et al.*, 1997). It also co-localizes with Mito-GFP and Mito-PAGFP (Chowdhary *et al.*, 2017).

DHE staining

ROS estimation of embryos was performed using dihydroethidium (DHE) (Molecular Probes, Lifetechnologies). DHE fluoresces when imaged at 561 nm upon oxidation due to the presence of ROS in the cells and is a quantitative readout for the amount of ROS. Embryos were fixed using Heptane: 4%PFA (1:1), washed with PBS, and incubated with 30nM DHE for 7 mins in PBS. The embryos were then washed with PBST, stained with Hoechst 33342 (Molecular Probes, 1:1000), and mounted on slides using Slowfade Gold (Life Technologies). The samples were imaged using Plan Apochromat 63x/1.4 NA, oil immersion objective on confocal laser scanning microscope (Zeiss, LSM 780) at the same laser and gain settings.

Image Analysis

Mean and Total Mitochondrial fluorescence intensity in Z stacks

Mean Mito-GFP intensity was measured in Z stacks with 1 μm increment in live Mito-GFP cellularizing embryos using ImageJ. The mean intensity was normalized to the highest intensity value in each set. The average of normalized intensities from 3 embryos was plotted with SEM using Graphpad Prism 5.0 (Figure 1C, 3D, S2C).

To estimate mitochondrial incorporation in cells as the furrow ingressed, mean Mito-GFP intensity was measured from sum projected Z stacks from apical to the section where furrow had reached during cellularization (Figure 1E, 3E). The intensity is plotted relative to the first cellularization time points of control and Drp1^{SG} (Figure 1E, 3E). Total Mito-GFP during cellularization was quantified by measuring the mean intensity of sum projected 40 Z stacks for each embryo across time in cellularization (Figure S1B).

Kymograph

A timelapse movie of photoactivated mitochondria in Mito-PA-GFP embryos was intensity thresholded and smoothed using ImageJ. A 2D Kymograph was plotted for a line ROI of 12 μm length and 2 μm thickness, drawn across the apicobasal axis in Mito-PAGFP embryos (Figure S1C).

Mitochondrial number quantification in EMs

Mitochondria in the EMs were identified based on structure and electron density. The number of electron dense particles in the cortical nuclei above the nuclei in each cell was counted manually for early, mid and late cellularization stage embryos. Total number of apical mitochondria per cell was plotted as mean with SEM using Graphpad prism 5.0 (Figure 1K).

Mitochondrial area measurement in apical and basal sections and relative mitochondrial area measurement in apical sections

Images obtained from fluorescently streptavidin stained embryos were intensity thresholded by subtracting 1.5 times the mean intensity value of single image plane and mean intensity of projected images for Z stacks. Fluorescent particles of size greater than $0.05 \mu\text{m}^2$ were marked using the “particle analyser” tool in ImageJ (Figure 3B, 6B, S3B). Mean particle size was obtained for each embryo. To estimate relative apical mitochondrial area (Figure 6C, S3C), the total area of threshold selected fluorescent particles was divided by area of the imaging field and expressed as a percentage. The data were plotted and analysed with Mann-Whitney test using Graphpad Prism 5.0.

pAMPK and DHE intensity quantification

Control and mutant embryos were processed and imaged at the same time using the same laser power and gain settings. Differences between the levels of pAMPK antibody signals (Figure 4B) and DHE fluorescence (Figure 4D) between control and experimental embryos were estimated based on fluorescence intensity. The mean intensities were measured from single planes using ImageJ. All intensity values in control and Drp1 were divided by the average of all the mean intensity values obtained for control embryos to get normalized values to represent as a fold change with respect to the control embryos and to show variability across control embryos. The data were plotted and compared with Mann-Whitney test using Graphpad Prism 5.0.

Furrow membrane length measurements in cellularization

Furrow membrane tips were identified by Sqh-mCherry or Sqh-GFP signal and the length from the apical plasma membrane was measured by using the line tool in ImageJ (Figure 1E, 2E, 5B, 5C, 7B, 7C, S4B, S4C). Readings were taken every 2 mins for 3-5 furrows in each embryo. Mean lengths with SEM were plotted across time using Graphpad Prism 5.0. The final lengths were compared using Mann-Whitney test on Graphpad Prism 5.0

Sqh-GFP and Sqh-mCherry fluorescence intensity and contractile ring area measurements

Identical laser power and gain settings were used for imaging control and experimental embryos. Sum intensity images for Sqh-mCherry or Sqh-GFP embryos (Figure 5E, 7E, S4E) were obtained for the basalmost optical sections showing brightest signal and 2 stacks above and below it (total Z depth - 4 μm). Mean fluorescence intensities of these projections were measured at different membrane ingression lengths using ImageJ and background corrected. A central region in a section below the nuclei containing uniform signal in the first cellularization time point (membrane length - 3 μm) was chosen to measure the background intensity (He *et al.*, 2016). The values obtained were normalized using average mean intensity value at 15 μm depth for control embryos in every imaging set, this is a point at which Myosin II intensity peaks during cellularization. Note that the same trend of relative fluorescence changes was seen in Sqh-mCherry and Sqh-GFP embryos (Figure S5). Normalized mean intensities across membrane lengths were plotted using Graphpad Prism 5.0.

Contractile ring area (Figure 5F, 5G, 7F, 7G, S4F, S4G) was measured at the basalmost membrane section from 5 contractile rings per embryo for fixed images or per time point for live samples. The ring area was marked manually in sum projection images of Sqh-mCherry or Sqh-GFP containing embryos using the polygon drawing tool in ImageJ. Average area was plotted with membrane length using Graphpad Prism 5.0. The final areas of contractile rings were compared using Mann-Whitney test on Graphpad Prism 5.0.

Acknowledgements

We thank Girish Ratnaparkhi for discussions on the data and manuscript. We thank RR lab members for their critical input on the data in the manuscript. We thank the IISER, Pune, *Drosophila* and Microscopy facilities for help with experiments. We thank Bloomington *Drosophila* stock center, Indiana, USA for stocks and DSHB, USA for antibodies. We thank Leo Pallanck for anti-Drp1 antibody. SC thanks UGC, SM thanks IISER, Pune, DT thanks UGC and RR thanks DBT, DST and IISER, Pune for funding. We thank J-P. Chauvin, A. Aouane and F. Richard at the IBDM electron microscopy facility (Marseille, France) for help with embryo processing and image acquisition.

References:

Afshar, K, Stuart, B, and Wasserman, SA (2000). Functional analysis of the *Drosophila* diaphanous FH protein in early embryonic development. *Development* 127, 1887–1897.

An, PNT, Yamaguchi, M, Bamba, T, and Fukusaki, E (2014). Metabolome analysis of *Drosophila melanogaster* during embryogenesis. *PLoS One* 9, e99519.

Arora, GK, Tran, SL, Rizzo, N, Jain, A, and Welte, MA (2016). Temporal control of bidirectional lipid-droplet motion in *Drosophila* depends on the ratio of kinesin-1 and its co-factor Halo. *Journal of Cell Science* 129, 1416–1428.

Bavister, BD, and Squirrell, JM (2000). Mitochondrial distribution and function in oocytes and early embryos. *Hum Reprod* 15 Suppl 2, 189–198.

Bell, EL, Klimova, TA, Eisenbart, J, Moraes, CT, Murphy, MP, Budinger, GRS, and Chandel, NS (2007). The Qo site of the mitochondrial complex III is required for the transduction of hypoxic signaling via reactive oxygen species production. *J Cell Biol* 177, 1029–1036.

van der Bliek, AM, Shen, Q, and Kawajiri, S (2013). Mechanisms of mitochondrial fission and fusion. *Cold Spring Harb Perspect Biol* 5.

Chen, C-T, Hsu, S-H, and Wei, Y-H (2012). Mitochondrial bioenergetic function and metabolic plasticity in stem cell differentiation and cellular reprogramming. *Biochim Biophys Acta* 1820, 571–576.

Chen, H, and Chan, DC (2009). Mitochondrial dynamics-fusion, fission, movement, and mitophagy-in neurodegenerative diseases. *Human Molecular Genetics* 18, R169–R176.

Chen, H, Detmer, SA, Ewald, AJ, Griffin, EE, Fraser, SE, and Chan, DC (2003). Mitofusins Mfn1 and Mfn2 coordinately regulate mitochondrial fusion and are essential for embryonic development. *J Cell Biol* 160, 189–200.

Choi, SY, Kim, JY, Kim, H-W, Cho, B, Cho, HM, Oppenheim, RW, Kim, H, Rhyu, IJ, and Sun, W (2013). Drp1-mediated mitochondrial dynamics and survival of developing chick motoneurons during the period of normal programmed cell death. *FASEB J* 27, 51–62.

Chowdhary, S, Tomer, D, Dubal, D, Sambre, D, and Rikhy, R (2017). Analysis of mitochondrial organization and function in the *Drosophila* blastoderm embryo. *Sci Rep* 7, 5502.

Cogliati, S et al. (2013). Mitochondrial cristae shape determines respiratory chain supercomplexes assembly and respiratory efficiency. *Cell* 155, 160–171.

Costa, V, Giacomello, M, Hudec, R, Lopreiato, R, Ermak, G, Lim, D, Malorni, W, Davies, KJA, Carafoli, E, and Scorrano, L (2010). Mitochondrial fission and cristae disruption increase the response of cell models of Huntington's disease to apoptotic stimuli. *EMBO Mol Med* 2, 490–503.

Das Gupta, PT, and Narasimha, M (2019). Cytoskeletal tension and Bazooka tune interface geometry to ensure fusion fidelity and sheet integrity during dorsal closure. *Elife* 8.

Dumollard, R, Duchen, M, and Carroll, J (2007). The role of mitochondrial function in the oocyte and embryo. *Curr Top Dev Biol* 77, 21–49.

Dumollard, R, Duchen, M, and Sardet, C (2006). Calcium signals and mitochondria at fertilisation. *Semin Cell Dev Biol* 17, 314–323.

Fedorova, M, Kuleva, N, and Hoffmann, R (2009). Reversible and irreversible modifications of skeletal muscle proteins in a rat model of acute oxidative stress. *Biochim Biophys Acta* 1792, 1185–1193.

Fiaschi, T, Cozzi, G, and Chiarugi, P (2012). Redox Regulation of Nonmuscle Myosin Heavy Chain during Integrin Engagement. *J Signal Transduct* 2012, 754964.

Field, CM, Coughlin, M, Doberstein, S, Marty, T, and Sullivan, W (2005). Characterization of anillin mutants reveals essential roles in septin localization and

plasma membrane integrity. *Development* 132, 2849–2860.

Figard, L, Xu, H, Garcia, HG, Golding, I, and Sokac, AM (2013). The plasma membrane flattens out to fuel cell-surface growth during *Drosophila* cellularization. *Dev Cell* 27, 648–655.

Fransson, S, Ruusala, A, and Aspenström, P (2006). The atypical Rho GTPases Miro-1 and Miro-2 have essential roles in mitochondrial trafficking. *Biochem Biophys Res Commun* 344, 500–510.

Frescas, D, Mavrakis, M, Lorenz, H, Delotto, R, and Lippincott-Schwartz, J (2006). The secretory membrane system in the *Drosophila* syncytial blastoderm embryo exists as functionally compartmentalized units around individual nuclei. *J Cell Biol* 173, 219–230.

Grosshans, J (2005). RhoGEF2 and the formin Dia control the formation of the furrow canal by directed actin assembly during *Drosophila* cellularisation. *Development* 132, 1009–1020.

Guo, X, Macleod, GT, Wellington, A, Hu, F, Panchumarthi, S, Schoenfield, M, Marin, L, Charlton, MP, Atwood, HL, and Zinsmaier, KE (2005). The GTPase dMiro is required for axonal transport of mitochondria to *Drosophila* synapses. *Neuron* 47, 379–393.

Hardie, DG, and Sakamoto, K (2006). AMPK: a key sensor of fuel and energy status in skeletal muscle. *Physiology* 21, 48–60.

He, B, Martin, A, and Wieschaus, E (2016). Flow-dependent myosin recruitment during *Drosophila* cellularization requires zygotic *dunk* activity. *Development* 143, 2417–2430.

Hollenbeck, PJ, and Saxton, WM (2005). The axonal transport of mitochondria. *J Cell Sci* 118, 5411–5419.

Hollinshead, M, Sanderson, J, and Vaux, DJ (1997). Anti-biotin antibodies offer superior organelle-specific labeling of mitochondria over avidin or streptavidin. *J Histochem Cytochem* 45, 1053–1057.

Hom, J, Yu, T, Yoon, Y, Porter, G, and Sheu, S-S (2010). Regulation of mitochondrial fission by intracellular Ca²⁺ in rat ventricular myocytes. *Biochim Biophys Acta* 1797, 913–921.

Hunter, MV, Willoughby, PM, Bruce, AEE, and Fernandez-Gonzalez, R (2018). Oxidative Stress Orchestrates Cell Polarity to Promote Embryonic Wound Healing. *Dev Cell* 47, 377–387.e4.

Ishihara, N et al. (2009). Mitochondrial fission factor Drp1 is essential for embryonic development and synapse formation in mice. *Nat Cell Biol* 11, 958–966.

Islam, R, Kumimoto, EL, Bao, H, and Zhang, B (2012). ALS-linked SOD1 in glial cells enhances β-N-Methylamino L-Alanine (BMAA)-induced toxicity in *Drosophila*. *F1000Res* 1, 47.

Ji, A-R, Ku, S-Y, Cho, MS, Kim, YY, Kim, YJ, Oh, SK, Kim, SH, Moon, SY, and Choi, YM (2010). Reactive oxygen species enhance differentiation of human embryonic stem cells into mesendodermal lineage. *Exp Mol Med* 42, 175–186.

Jordan, P, and Karess, R (1997). Myosin Light Chain-activating Phosphorylation Sites Are Required for Oogenesis in *Drosophila*. *J Cell Biol* 139, 1805–1819.

Karr, TL, and Alberts, BM (1986). Organization of the cytoskeleton in early *Drosophila* embryos. *J Cell Biol* 102, 1494–1509.

Kimura, K et al. (1996). Regulation of Myosin Phosphatase by Rho and Rho-Associated Kinase (Rho-Kinase). *Science* 273, 245–248.

Kim, Y-M et al. (2018). Redox Regulation of Mitochondrial Fission Protein Drp1 by Protein Disulfide Isomerase Limits Endothelial Senescence. *Cell Rep* 23, 3565–3578.

Krueger, D, Tardivo, P, Nguyen, C, and De Renzis, S (2018). Downregulation of basal myosin-II is required for cell shape changes and tissue invagination. *EMBO J* 37.

Kuhlmann, CRW, Tamaki, R, Gamerdinger, M, Lessmann, V, Behl, C, Kempster, OS,

and Luhmann, HJ (2007). Inhibition of the myosin light chain kinase prevents hypoxia-induced blood-brain barrier disruption. *J Neurochem* 102, 501–507.

Lecuit, T, and Wieschaus, E (2000). Polarized insertion of new membrane from a cytoplasmic reservoir during cleavage of the *Drosophila* embryo. *J Cell Biol* 150, 849–860.

Liu, Y, Fiskum, G, and Schubert, D (2002). Generation of reactive oxygen species by the mitochondrial electron transport chain. *Journal of Neurochemistry* 80, 780–787.

Li, Z, Okamoto, K-I, Hayashi, Y, and Sheng, M (2004). The importance of dendritic mitochondria in the morphogenesis and plasticity of spines and synapses. *Cell* 119, 873–887.

Mavrakis, M, Azou-Gros, Y, Tsai, F-C, Alvarado, J, Bertin, A, Iv, F, Kress, A, Brasselet, S, Koenderink, GH, and Lecuit, T (2014). Septins promote F-actin ring formation by crosslinking actin filaments into curved bundles. *Nat Cell Biol* 16, 322–334.

Mazumdar, A, and Mazumdar, M (2002). How one becomes many: blastoderm cellularization in *Drosophila melanogaster*. *Bioessays* 24, 1012–1022.

Mehta, K, Chacko, LA, Chug, MK, Jhunjhunwala, S, and Ananthanarayanan, V (2019). Association of mitochondria with microtubules inhibits mitochondrial fission by precluding assembly of the fission protein Dnm1. *J Biol Chem* 294, 3385–3396.

Melkov, A, Baskar, R, Alcalay, Y, and Abdu, U (2016). A new mode of mitochondrial transport and polarized sorting regulated by Dynein, Milton and Miro. *Development* 143, 4203–4213.

Merrill, PT, Sweeton, D, and Wieschaus, E (1988). Requirements for autosomal gene activity during precellular stages of *Drosophila melanogaster*. *Development* 104, 495–509.

Mironov, SL, and Symonchuk, N (2006). ER vesicles and mitochondria move and communicate at synapses. *J Cell Sci* 119, 4926–4934.

Mishra, AK, Mondo, JA, Campanale, JP, and Montell, DJ (2019). Coordination of protrusion dynamics within and between collectively migrating border cells by myosin II. *Mol Biol Cell* 30, 2490–2502.

Mishra, P, and Chan, DC (2016). Metabolic regulation of mitochondrial dynamics. *J Cell Biol* 212, 379–387.

Mitra, K, Rikhy, R, Lilly, M, and Lippincott-Schwartz, J (2012). DRP1-dependent mitochondrial fission initiates follicle cell differentiation during *Drosophila* oogenesis. *J Cell Biol* 197, 487–497.

Moore, BA, Gonzalez Aviles, GD, Larkins, CE, Hillman, MJ, and Casparly, T (2010). Mitochondrial retention of Opa1 is required for mouse embryogenesis. *Mamm Genome* 21, 350–360.

Morlino, G et al. (2014). Miro-1 Links Mitochondria and Microtubule Dynein Motors To Control Lymphocyte Migration and Polarity. *Molecular and Cellular Biology* 34, 1412–1426.

Morris, RL, and Hollenbeck, PJ (1993). The regulation of bidirectional mitochondrial transport is coordinated with axonal outgrowth. *J Cell Sci* 104 (Pt 3), 917–927.

Muliyil, S, and Narasimha, M (2014). Mitochondrial ROS regulates cytoskeletal and mitochondrial remodeling to tune cell and tissue dynamics in a model for wound healing. *Dev Cell* 28, 239–252.

Papoulas, O, Hays, TS, and Sisson, JC (2005). The golgin Lava lamp mediates dynein-based Golgi movements during *Drosophila* cellularization. *Nat Cell Biol* 7, 612–618.

Pepling, ME, and Spradling, AC (2001). Mouse ovarian germ cell cysts undergo programmed breakdown to form primordial follicles. *Dev Biol* 234, 339–351.

Rawson, RL, Yam, L, Weimer, RM, Bend, EG, Hartweg, E, Robert Horvitz, H, Clark, SG, and Jorgensen, EM (2014). Axons Degenerate in the Absence of Mitochondria in *C. elegans*. *Current Biology* 24, 760–765.

Rice, SE, and Gelfand, VI (2006). Paradigm lost: Milton connects kinesin heavy chain to Miro on mitochondria. *J Cell Biol* 173, 459–461.

Rikhy, R, Kamat, S, Ramagiri, S, Sriram, V, and Krishnan, KS (2007). Mutations in dynamin-related protein result in gross changes in mitochondrial morphology and affect synaptic vesicle recycling at the *Drosophila* neuromuscular junction. *Genes Brain Behav* 6, 42–53.

Röth, D, Krammer, PH, and Gülow, K (2014). Dynamin related protein 1-dependent mitochondrial fission regulates oxidative signalling in T cells. *FEBS Letters* 588, 1749–1754.

Royou, A, Field, C, Sisson, JC, Sullivan, W, and Karess, R (2004). Reassessing the role and dynamics of nonmuscle myosin II during furrow formation in early *Drosophila* embryos. *Mol Biol Cell* 15, 838–850.

Royou, A, Sullivan, W, and Karess, R (2002). Cortical recruitment of nonmuscle myosin II in early syncytial *Drosophila* embryos: its role in nuclear axial expansion and its regulation by Cdc2 activity. *J Cell Biol* 158, 127–137.

Russo, GJ, Louie, K, Wellington, A, Macleod, GT, Hu, F, Panchumarthi, S, and Zinsmaier, KE (2009). *Drosophila* Miro is required for both anterograde and retrograde axonal mitochondrial transport. *J Neurosci* 29, 5443–5455.

Sakamoto, K, McCarthy, A, Smith, D, Green, KA, Grahame Hardie, D, Ashworth, A, and Alessi, DR (2005). Deficiency of LKB1 in skeletal muscle prevents AMPK activation and glucose uptake during contraction. *EMBO J* 24, 1810–1820.

Saotome, M, Safiulina, D, Szabadkai, G, Das, S, Fransson, A, Aspenstrom, P, Rizzuto, R, and Hajnóczky, G (2008). Bidirectional Ca²⁺-dependent control of mitochondrial dynamics by the Miro GTPase. *Proc Natl Acad Sci U S A* 105, 20728–20733.

Sathananthan, AH, and Trounson, AO (2000). Mitochondrial morphology during preimplantational human embryogenesis. *Hum Reprod* 15 Suppl 2, 148–159.

Saxton, WM, and Hollenbeck, PJ (2012). The axonal transport of mitochondria. *J Cell Sci* 125, 2095–2104.

Schejter, ED, and Wieschaus, E (1993). bottleneck acts as a regulator of the microfilament network governing cellularization of the *Drosophila* embryo. *Cell* 75, 373–385.

Schwarz, TL (2013). Mitochondrial trafficking in neurons. *Cold Spring Harb Perspect Biol* 5.

Sen, A, Nagy-Zsvér-Vadas, Z, and Krahn, MP (2012). *Drosophila* PATJ supports adherens junction stability by modulating Myosin light chain activity. *J Cell Biol* 199, 685–698.

Shubeita, GT, Tran, SL, Xu, J, Vershinin, M, Cermelli, S, Cotton, SL, Welte, MA, and Gross, SP (2008). Consequences of motor copy number on the intracellular transport of kinesin-1-driven lipid droplets. *Cell* 135, 1098–1107.

Sisson, JC, Field, C, Ventura, R, Royou, A, and Sullivan, W (2000). Lava lamp, a novel peripheral golgi protein, is required for *Drosophila melanogaster* cellularization. *J Cell Biol* 151, 905–918.

Son, MJ, Kwon, Y, Son, M-Y, Seol, B, Choi, H-S, Ryu, S-W, Choi, C, and Cho, YS (2015). Mitofusins deficiency elicits mitochondrial metabolic reprogramming to pluripotency. *Cell Death Differ* 22, 1957–1969.

Steinberg, SF (2013). Oxidative Stress and Sarcomeric Proteins. *Circulation Research* 112, 393–405.

Strong, TC, and Thomas, JH (2011). Maternal and zygotic requirements for src64 during *Drosophila* cellularization. *Genesis* 49, 912–918.

Thomas, JH, and Wieschaus, E (2004). src64 and tec29 are required for microfilament contraction during *Drosophila* cellularization. *Development* 131, 863–871.

Toyama, EQ et al. (2016). Metabolism. AMP-activated protein kinase mediates mitochondrial fission in response to energy stress. *Science* 351, 275–281.

Tsushima, K et al. (2018). Mitochondrial Reactive Oxygen Species in Lipotoxic Hearts Induce Post-Translational Modifications of AKAP121, DRP1, and OPA1 That Promote Mitochondrial Fission. *Circ Res* 122, 58–73.

Ukeshima, A, and Fujimoto, T (1984). Ultrastructure of primordial germ cells in the early chick embryo. *Ultrastructure of Reproduction*, 12–18.

Van Blerkom, J, Davis, P, Mathwig, V, and Alexander, S (2002). Domains of high-polarized and low-polarized mitochondria may occur in mouse and human oocytes and early embryos. *Hum Reprod* 17, 393–406.

Vasquez, CG, Tworoger, M, and Martin, AC (2014). Dynamic myosin phosphorylation regulates contractile pulses and tissue integrity during epithelial morphogenesis. *J Cell Biol* 206, 435–450.

Verstreken, P, Ly, CV, Venken, KJT, Koh, T-W, Zhou, Y, and Bellen, HJ (2005). Synaptic mitochondria are critical for mobilization of reserve pool vesicles at *Drosophila* neuromuscular junctions. *Neuron* 47, 365–378.

Wakabayashi, J, Zhang, Z, Wakabayashi, N, Tamura, Y, Fukaya, M, Kensler, TW, Iijima, M, and Sesaki, H (2009). The dynamin-related GTPase Drp1 is required for embryonic and brain development in mice. *J Cell Biol* 186, 805–816.

Wang, X, and Schwarz, TL (2009). The Mechanism of Ca²⁺-Dependent Regulation of Kinesin-Mediated Mitochondrial Motility. *Cell* 136, 163–174.

Wang, X, Winter, D, Ashrafi, G, Schlehe, J, Wong, YL, Selkoe, D, Rice, S, Steen, J, LaVoie, MJ, and Schwarz, TL (2011). PINK1 and Parkin target Miro for phosphorylation and degradation to arrest mitochondrial motility. *Cell* 147, 893–906.

Warn, RM, and Magrath, R (1983). F-actin distribution during the cellularization of the *Drosophila* embryo visualized with FL-phalloidin. *Exp Cell Res* 143, 103–114.

Warn, RM, and Robert-Nicoud, M (1990). F-actin organization during the cellularization of the *Drosophila* embryo as revealed with a confocal laser scanning microscope. *J Cell Sci* 96 (Pt 1), 35–42.

Watson, MR, Lagow, RD, Xu, K, Zhang, B, and Bonini, NM (2008). A *drosophila* model for amyotrophic lateral sclerosis reveals motor neuron damage by human SOD1. *J Biol Chem* 283, 24972–24981.

Welte, MA, Gross, SP, Postner, M, Block, SM, and Wieschaus, EF (1998). Developmental regulation of vesicle transport in *Drosophila* embryos: forces and kinetics. *Cell* 92, 547–557.

Wenzl, C, Yan, S, Laupsien, P, and Grosshans, J (2010). Localization of RhoGEF2 during *Drosophila* cellularization is developmentally controlled by Slam. *Mech Dev* 127, 371–384.

Wilding, M, Carotenuto, R, Infante, V, Dale, B, Marino, M, Di Matteo, L, and Campanella, C (2001). Confocal microscopy analysis of the activity of mitochondria contained within the “mitochondrial cloud” during oogenesis in *Xenopus laevis*. *Zygote* 9, 347–352.

Xue, Z, and Sokac, AM (2016). -Back-to-back mechanisms drive actomyosin ring closure during *Drosophila* embryo cleavage. *J Cell Biol* 215, 335–344.

Yaffe, MP, Harata, D, Verde, F, Eddison, M, Toda, T, and Nurse, P (1996). Microtubules mediate mitochondrial distribution in fission yeast. *Proc Natl Acad Sci U S A* 93, 11664–11668.

Young, PE, Pesacreta, TC, and Kiehart, DP (1991). Dynamic changes in the distribution of cytoplasmic myosin during *Drosophila* embryogenesis. *Development* 111, 1–14.

Yu, T, Robotham, JL, and Yoon, Y (2006). Increased production of reactive oxygen species in hyperglycemic conditions requires dynamic change of mitochondrial morphology. *Proc Natl Acad Sci U S A* 103, 2653–2658.

Zhang, Y, Yu, JC, Jiang, T, Fernandez-Gonzalez, R, and Harris, TJC (2018). Collision of Expanding Actin Caps with Actomyosin Borders for Cortical Bending and Mitotic Rounding in a Syncytium. *Dev Cell* 45, 551–564.e4.

Zhang, Y-Z, Ouyang, Y-C, Hou, Y, Schatten, H, Chen, D-Y, and Sun, Q-Y (2008). Mitochondrial behavior during oogenesis in zebrafish: a confocal microscopy analysis. *Dev Growth Differ* 50, 189–201.

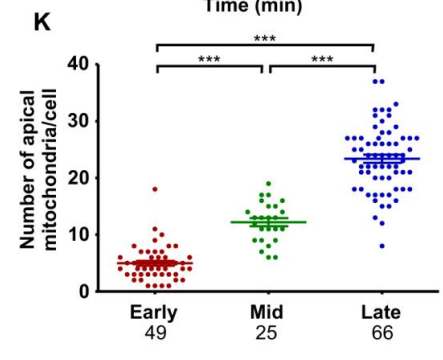
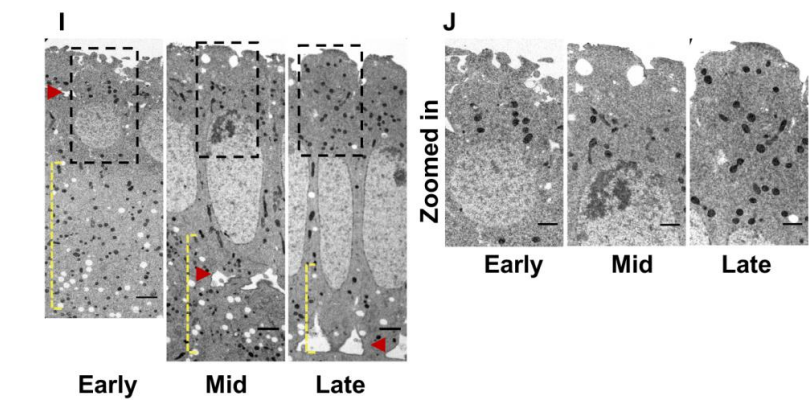
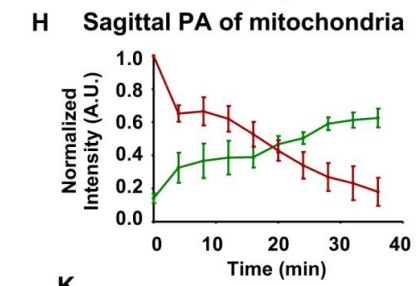
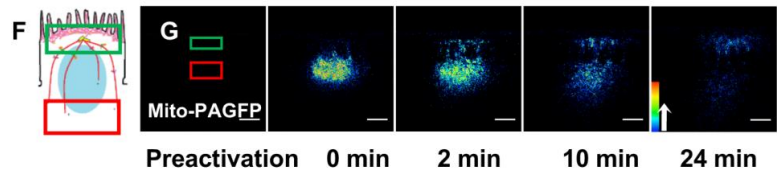
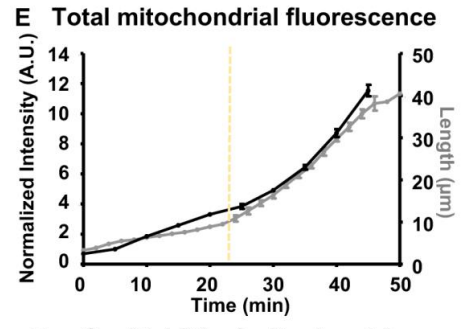
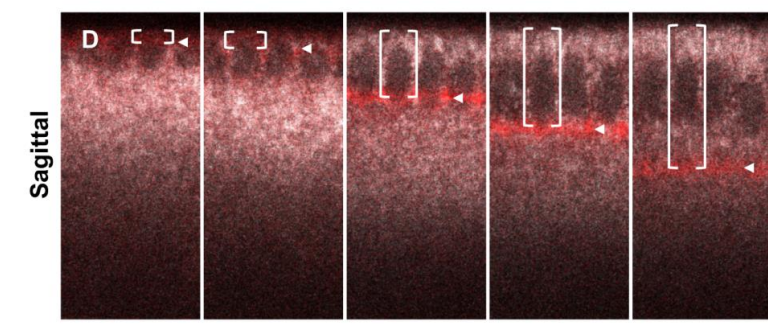
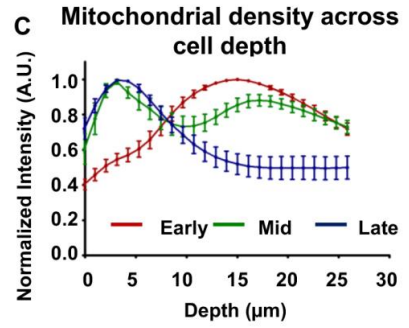
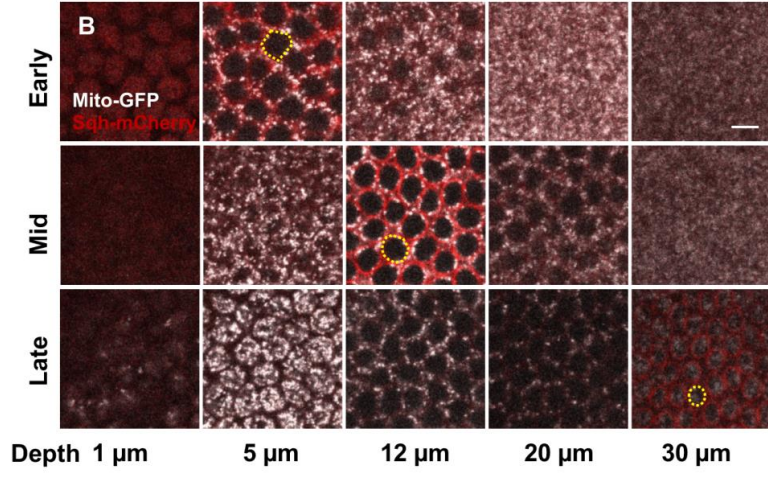
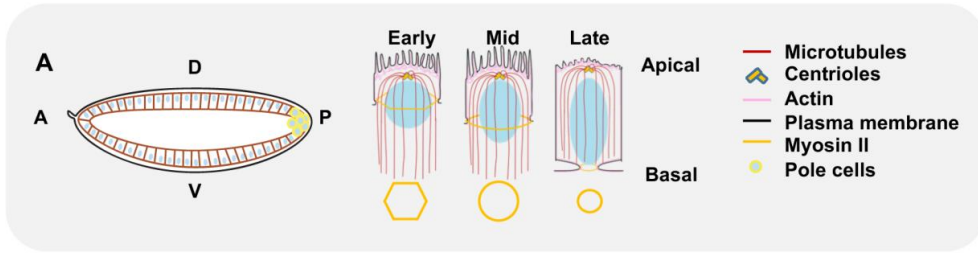


Figure 1: Mitochondria accumulate in apical regions above nuclei during cellularization

(A) Schematic showing the *Drosophila* embryo at the end of cellularization with a single layer of epithelial cells at the cortex. The plasma membrane extends basally during cellularization and microtubules (**red**) emanate from apical centrosomes. Early, mid and late stages represent successive increase in plasma membrane (**black**) length and change in furrow architecture at the base from polygonal (at early) to circular (at mid) followed by constriction (at late). Myosin II (**yellow**) is present at the furrow and gets enriched during mid cellularization.

(B-K) Mitochondria enrich apically during cellularization. Optical sections at depths represented for early, mid and late cellularization obtained from live imaging of embryos expressing Mito-GFP (**grey**) and Sqh-mCherry (**red**) show increase in MitoGFP (**grey**) signal in apical sections (**5 μm**) during mid and late cellularization. Membrane extension during these stages is visualized using Sqh-mCherry (**red**) and is marked by yellow dotted lines (**B**). Mean fluorescence intensity of Mito-GFP is quantified across optical sections in 1 μm depth increments and plotted with depth at early (**red**), mid (**green**) and late cellularization (**blue**) $n = 3$ embryos, 200 cells (**C**). Sagittal images of Mito-GFP, Sqh-mCherry embryos at represented membrane ingression lengths (**arrowheads**) show increase in apical mitochondrial fluorescence and their presence along the ingressing furrow (**D**). Total Mito-GFP fluorescence intensity above the furrow tips (**D; bracketed region, E; black, left Y-axis**) plotted along with membrane ingression (**grey, right Y-axis**) across time display slow and fast phases. The transition point between slow and fast phases is marked with a yellow dotted line. $n = 4$ embryos (approximately 40 cells each), 3 embryos (5 furrows each) for mitochondrial intensity and membrane ingression measurements respectively (**E**).

(F-H) Apical translocation of mitochondria is observed using photoactivation. Schematic of photoactivation shows photoactivated basal ROI (**red**) and non-photoactivated apical ROI (**green**) (**F**). A rainbow coloured intensity scale is used to depict the sagittal images showing photoactivation of Mito-PAGFP at the basal ROI (**red**) during early cellularization. The mean fluorescence intensity decreases at the basal region (**red**) and increases at the apical region (**green**) with time during cellularization (**G, H**). Normalized

mean fluorescence intensity is plotted for basal (**red**) and apical (**green**) regions for n = 4 embryos (approximately 3 cells each) across time (**H**).

(**I-K**) Transmission electron microscopy images of early, mid and late cellularization stages show punctate mitochondria (**I**). Embryo stages are identified by furrow length (**I**, **furrow tips - red arrowheads**). Basal regions are marked by yellow dashed lines.

Number of mitochondria in the apical region per section (**I**; **black rectangle, K**) increases gradually from early (**red, K**) to mid (**green, K**) and late (**blue, K**) cellularization. n = 3, 4, 4 embryos and total 49, 26, 66 cells for early, mid and late stages respectively are quantified. (***) P ≤ 0.001, Mann Whitney test). Scale Bar = 5 μm (**B, D and G**); 2 μm (**I**); 1 μm (**J**)

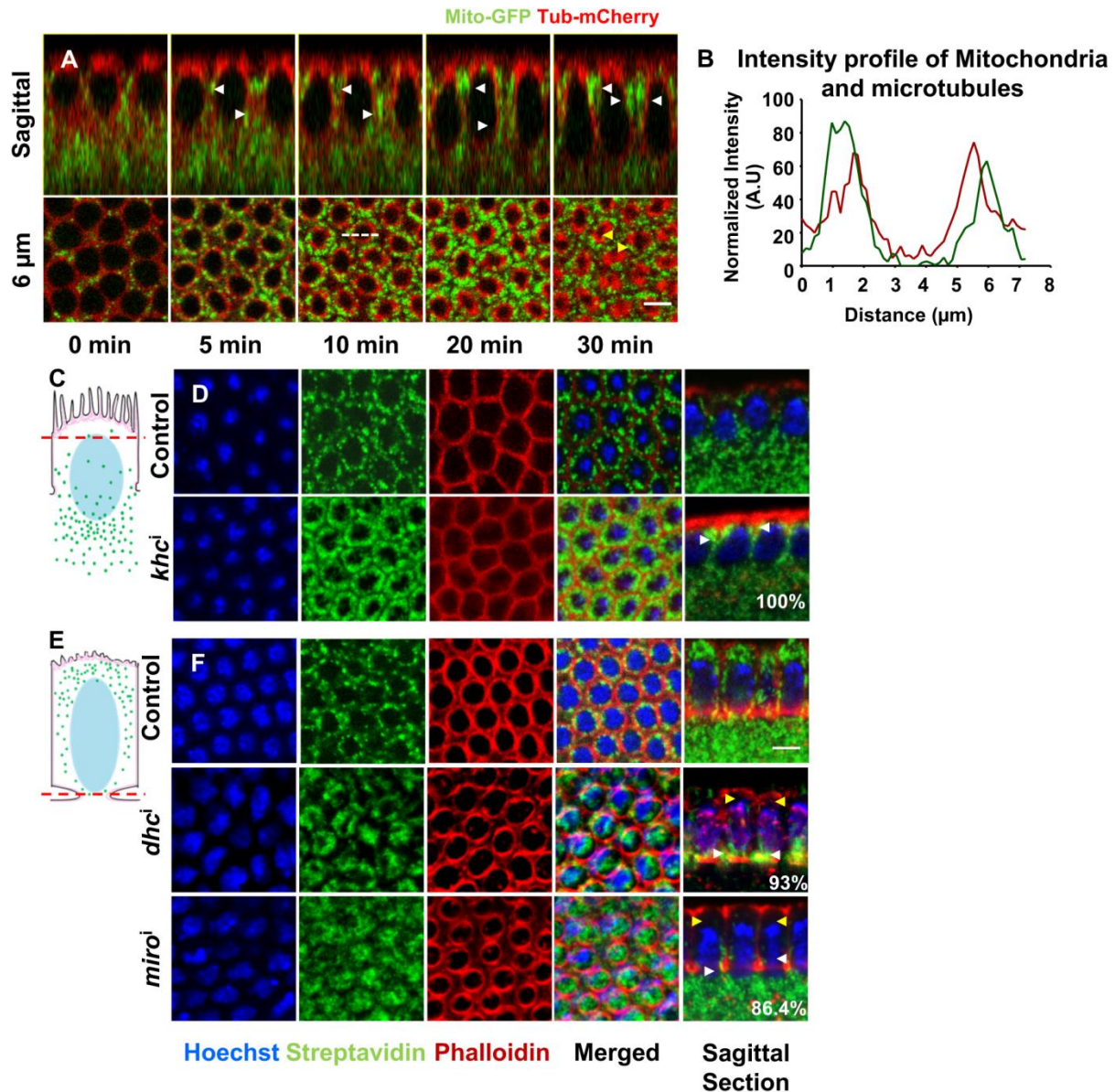


Figure 2: Apical transport of mitochondria occurs on microtubules

(A-B): Mitochondria localize adjacent to microtubules. Live imaging using Mito-GFP and Tub-mCherry shows mitochondria (green) colocalizing with microtubule tracks (red) during cellularization progression (white arrowheads) (A, sagittal). Mitochondria also accumulate around the centrioles (yellow arrowheads) (A, 6 μ m). Intensity profile of Mito-GFP (green) and Tub-mCherry (red) plotted for the region shown by white dashed line (A, 6 μ m, 10 mins) shows an overlap (B).

(C-F): Mitochondrial localization changes on depletion of microtubule motors. Mitochondrial (streptavidin, green) localization at subapical regions (Schematic, C,

red dotted line) around nuclei (**Hoechst, blue**) is compared between control and *khc*ⁱ embryos in early cellularization (**C-D**). Increased mitochondrial fluorescence in *khc*ⁱ embryos (100%, n = 24 embryos, early cellularization) (**D**) is also seen in sagittal image (**D, sagittal, white arrowheads**). Mitochondria (streptavidin, green) are clustered at the basal sections near the contractile rings (phalloidin, red) in late cellularization (**Schematic, E**) in 93% of *dhc*ⁱ (n = 32 embryos) and 86.4 % of *miro*ⁱ (n = 22 embryos) as compared to control embryos (**F, white arrowheads, sagittal**). Absence of apical mitochondria is denoted by **yellow arrowheads** in *dhc*ⁱ and *miro*ⁱ embryos (**F, sagittal**). Scale Bar = 5 μm (**A, D-F**).

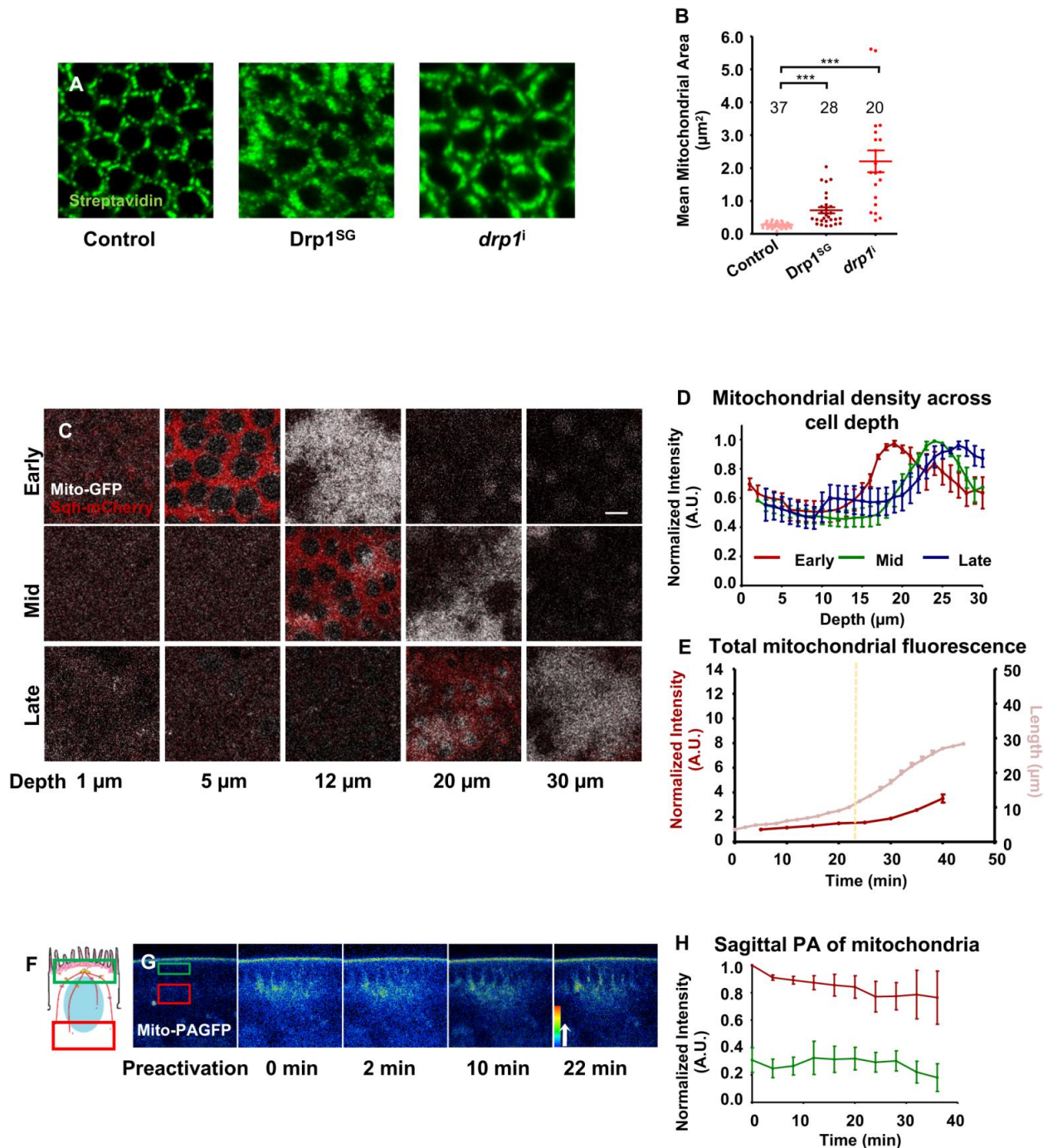


Figure 3: Apical translocation of mitochondria is decreased in *Drp1^{SG}*

(A-B): *Drp1* mutant embryos have clustered mitochondria. Mitochondria (**green**) labelled using fluorescent streptavidin are clustered in *Drp1^{SG}* and *drp1ⁱ* embryos compared to control Mito-GFP embryos (**A**). Optically resolvable mitochondrial area per embryo is quantified (**B**). Mitochondrial sizes are significantly larger in *Drp1^{SG}* (**deep red**) and *drp1ⁱ* (**red**) embryos compared to Mito-GFP (**light red**) embryos (**B**). Each

data point represents mean mitochondrial size from one embryo. $n = 37, 28$ and 20 embryos for control, Drp1^{SG} and drp1^i respectively, approximately 40 cells and 15000 optically resolvable fluorescent mitochondrial spots were counted per embryo (***, $P \leq 0.001$, Mann Whitney test) **(B)**. Scale bar: $5 \mu\text{m}$ **(A)**

(C-H): Apical mitochondrial translocation is reduced in Drp1^{SG} embryos. Live imaging of Mito-GFP containing Drp1^{SG} embryos shows mitochondrial clusters in basal regions of cells in early **(C, Top panel)**, mid **(C, Middle panel)** and late cellularization **(C, Bottom panel)**. Mitochondria are missing in the apical regions **(C)**. Sqh-mCherry signal is a readout of the membrane length at each time point. Mean Mito-GFP fluorescence across depth is plotted with SEM for $n = 3$ embryos and a total of 200 cells for early, mid and late cellularization stages **(D)**. Mito-GFP fluorescence peaks in basal regions at early (red), mid (green) and late (blue) cellularization stages **(D)**. Total intensity of Mito-GFP signal above the furrow is plotted with membrane length across time during cellularization. Yellow dotted line represents the slow-fast phase transition time point. **(E)**. Scale bar: $5 \mu\text{m}$ **(C)**

(F-H): Absence of apical translocation of mitochondria in Drp1^{SG} embryos is observed using photoactivation. Schematic of photoactivation experiment showing basal photoactivated ROI **(red)** and non-photoactivated apical ROI **(green)** **(F)**. Sagittal images of Mito-PAGFP containing Drp1^{SG} embryos, represented with rainbow intensity colour map, show no change in the localization of activated Mito-PAGFP signal at the basal regions **(red)** and the apical region **(green)** does not gain significant fluorescence signal with time during cellularization **(G)**. Normalized mean fluorescence intensity plotted with SEM for the basal **(red)** and apical regions **(green)** for $n = 3$ embryos (Approximately 3 cells each) shows no change across time **(H)**. Scale bar: $10 \mu\text{m}$ **(G)**

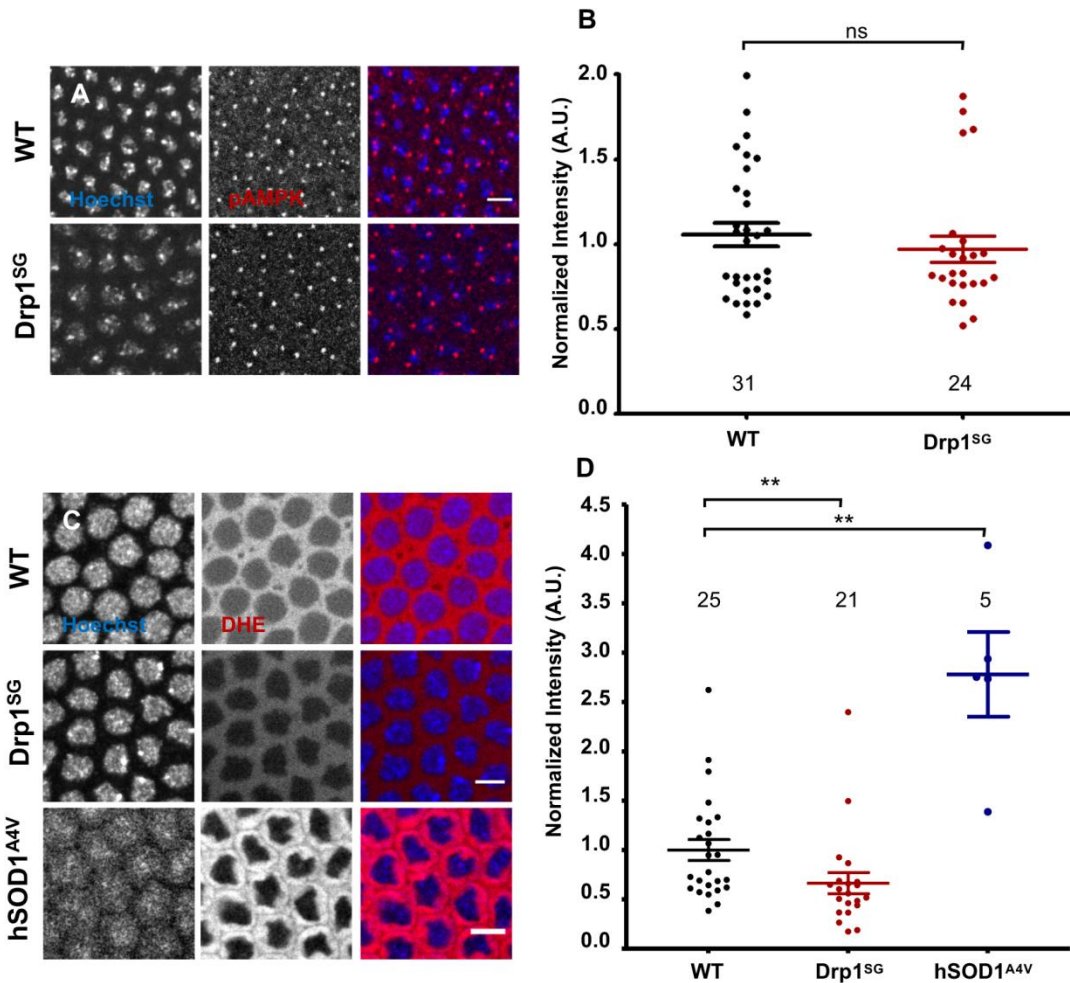


Figure 4: pAMPK levels are unchanged and ROS levels are reduced in Drp1^{SG} embryos

pAMPK (red) signal localizes to the cytoplasm around the nuclei (Hoechst, blue) and on punctae on either side of the nucleus in control and Drp1^{SG} embryos as seen in single plane sections at subapical regions (A). The mean normalized pAMPK fluorescence intensity levels quantified at represented single plane sections are comparable in control (black, B) and Drp1^{SG} (red, B) embryos.

ROS measured using DHE staining (red) has cytoplasmic signals in control, Drp1^{SG} and hSOD1^{A4V} embryos. Single plane sections through the nuclei are shown (C). Mean fluorescence intensity of DHE quantified at represented single plane sections is significantly reduced in Drp1^{SG} (red, D) and increased in the positive control, hSOD1^{A4V} (blue), compared to control (black, D) embryos (D). Number of independent experiments (N) = 3, and 2 for B, D respectively. Numbers on the graph represent the embryos analysed for each data set. (ns; P ≥ 0.05, **; P ≤ 0.01, Mann Whitney test). Scale bar: 5 μm (A, C).

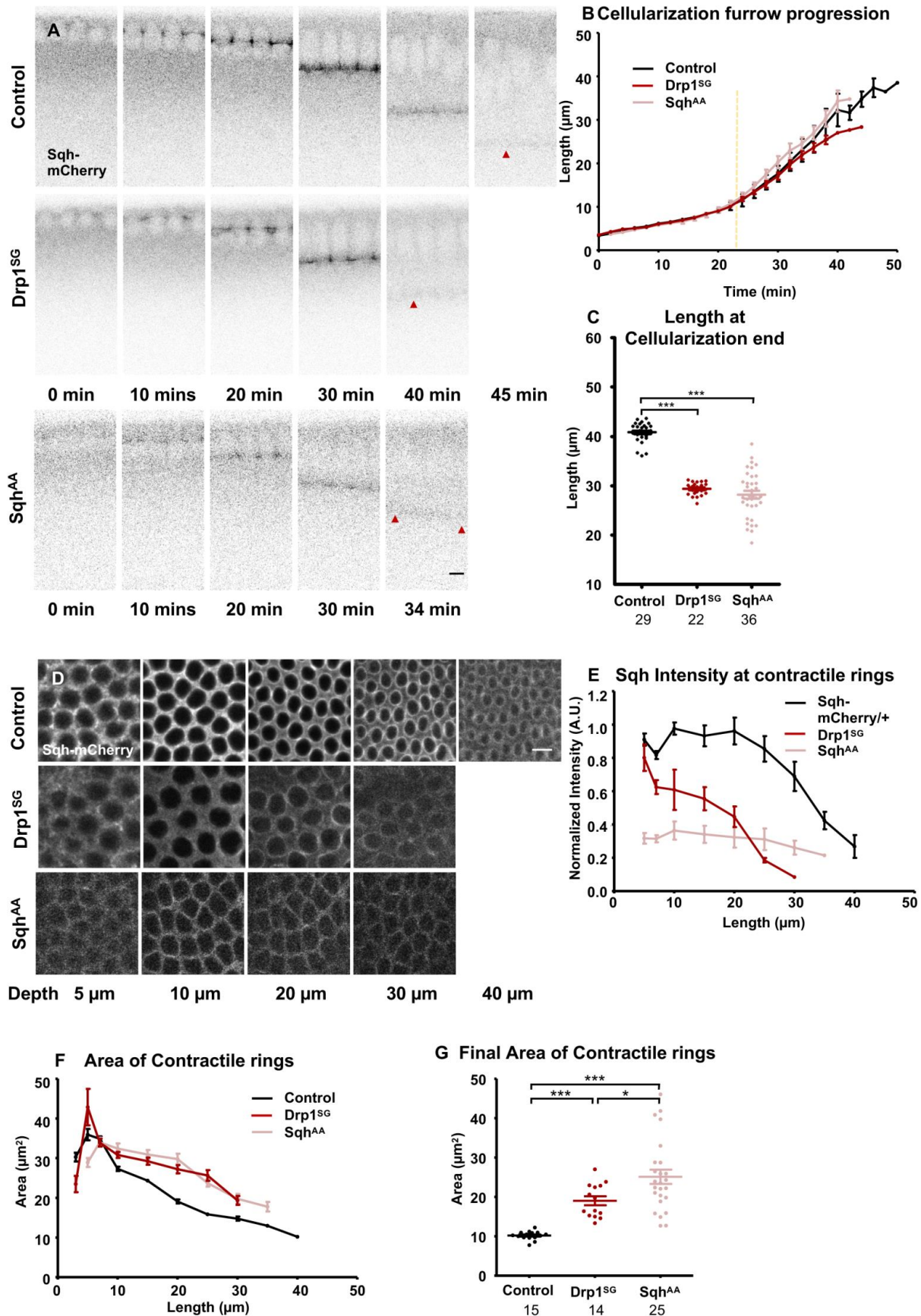


Figure 5: Drp1^{SG} embryos have shorter cells, decreased Myosin II and decreased area of contractile rings.

(A-C): Drp1^{SG} embryos have shorter cells at the end of cellularization. Sqh-mCherry expressing control, Drp1^{SG} and Sqh^{AA} embryos are imaged in the sagittal plane. Sqh-mCherry, localized to the membrane tips, shows the extent of membrane ingression during cellularization **(A)**. Membrane length quantified across time during cellularization shows a similar trend of the slow and fast phase of ingression in control **(black)**, Drp1^{SG} **(red)** and Sqh^{AA} **(light red)** **(B)**. The plots for control and Drp1^{SG} are repeated from Figure 1E and 3E respectively for comparison. Final cell length achieved post cellularization **(A, red arrowheads)** in Drp1^{SG} **(red)** and Sqh^{AA} **(light red)** is significantly smaller compared to control **(black)** **(A, C)**. $n = 4, 3, 6$ embryos (5 furrows each) **(B)**; 6, 5 and 7 embryos **(C)** for control, Drp1^{SG} and Sqh^{AA} respectively. Numbers on the plot represent total furrows analyzed for each data set **(C)**. (***) $P \leq 0.001$, Mann Whitney test) **(C)**. Scale bar: 5 μm **(A)**.

(D-G): Drp1^{SG} embryos have lowered Sqh levels. Sections through the cellularization furrow tips at mentioned furrow depths in Sqh-mCherry containing control and Drp1^{SG} embryos have decreasing contractile ring sizes with membrane depth **(D)**. Sqh^{AA} embryos show polygonal plasma membrane organization throughout **(D)**. Normalized mean intensity of Sqh-mCherry at the contractile rings during cellularization is significantly reduced in Drp1^{SG} **(red)** and Sqh^{AA} **(light red)** compared to control embryos **(black)** **(E)**. Area of contractile rings quantified across membrane depth in Drp1^{SG} **(red)** and Sqh^{AA} **(light red)** is larger than that in control embryos, **(black)** **(F)** with final areas for Drp1^{SG} **(red)** and Sqh^{AA} **(light red)** being significantly larger than the control **(black)** **(G)**. $n = 5, 4, 5$ embryos for control, Drp1^{SG} and Sqh^{AA} respectively, approximately 40 cells per embryo are quantified **(E)**. $n = 3, 3, 5$ embryos, 5 contractile rings per embryo for control, Drp1^{SG} and Sqh^{AA} respectively **(F, G)** are quantified at 5 μm length increments **(F)**. Number of rings quantified are represented in the plot **(G)**. (*; $P \leq 0.05$, ***) $P \leq 0.001$, Mann Whitney test) **(G)**. Scale bar: 5 μm **(D)**.

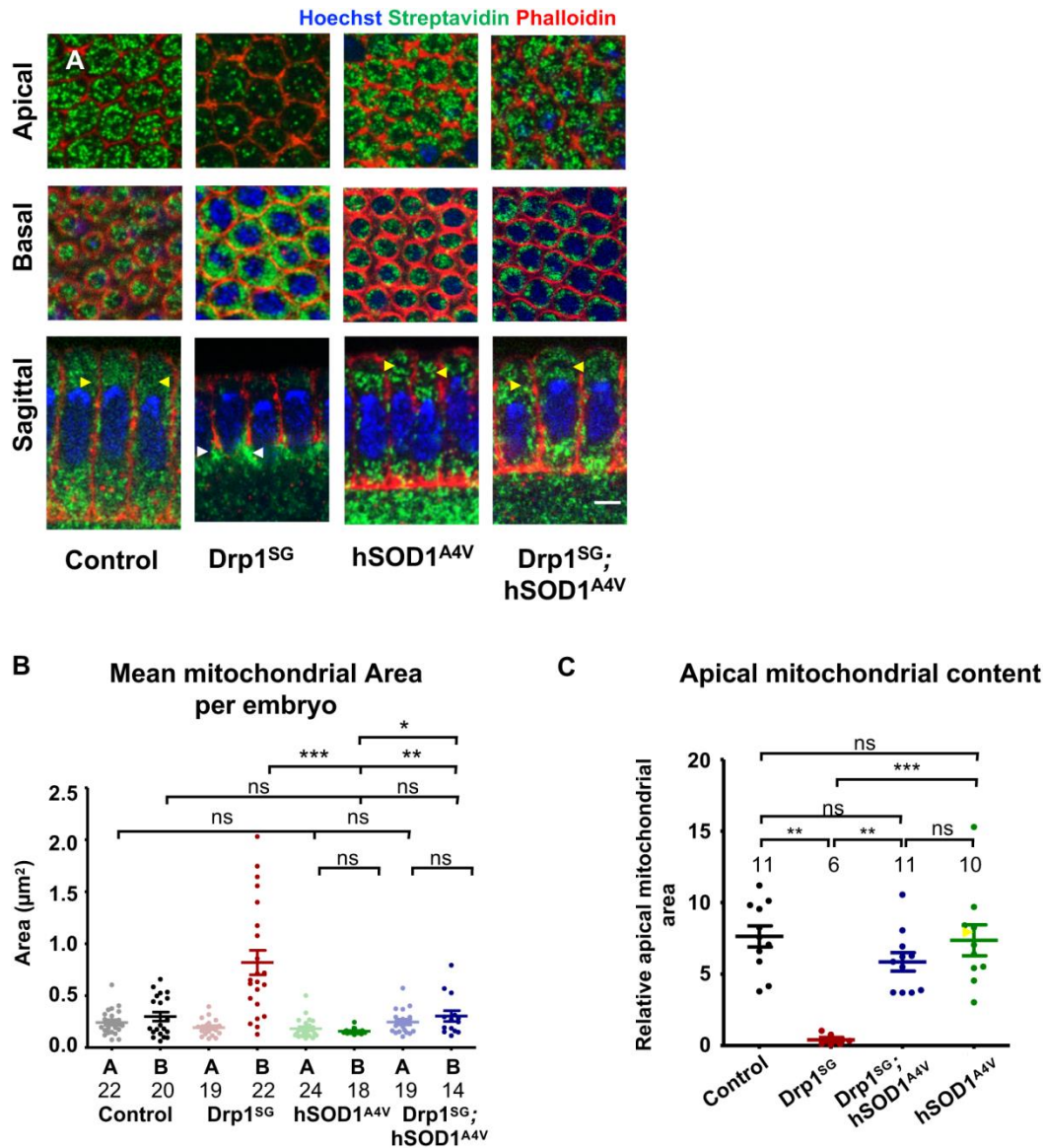
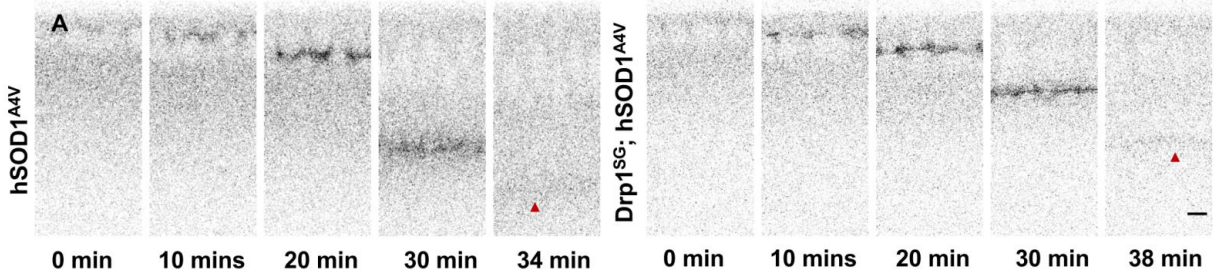


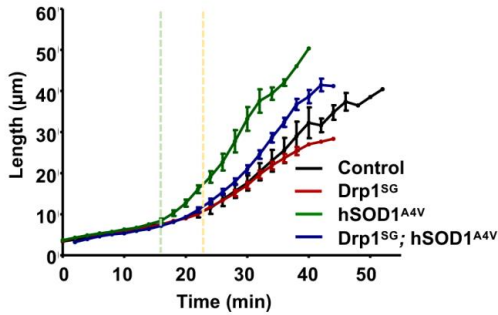
Figure 6: Mitochondrial shape and translocation defects in Drp1^{SG} are suppressed in Drp1^{SG}; hSOD1^{A4V} embryos

Small punctate mitochondria (**streptavidin, green**) are observed at the apical and basal regions, near contractile rings, (**phalloidin red**) in mid-late cellularization stage hSOD1^{A4V} and Drp1^{SG}; hSOD1^{A4V} embryos. Apical mitochondria are also seen in sagittal sections (**A, yellow arrowheads**). Mean mitochondrial size per embryo quantified in apical and basal sections of hSOD1^{A4V} (**green**) and Drp1^{SG}; hSOD1^{A4V} (**blue**) embryos is not significantly different compared to controls (**black**) (**B**). Mean mitochondrial area at the basal regions of hSOD1^{A4V} (**green**) and Drp1^{SG}; hSOD1^{A4V}

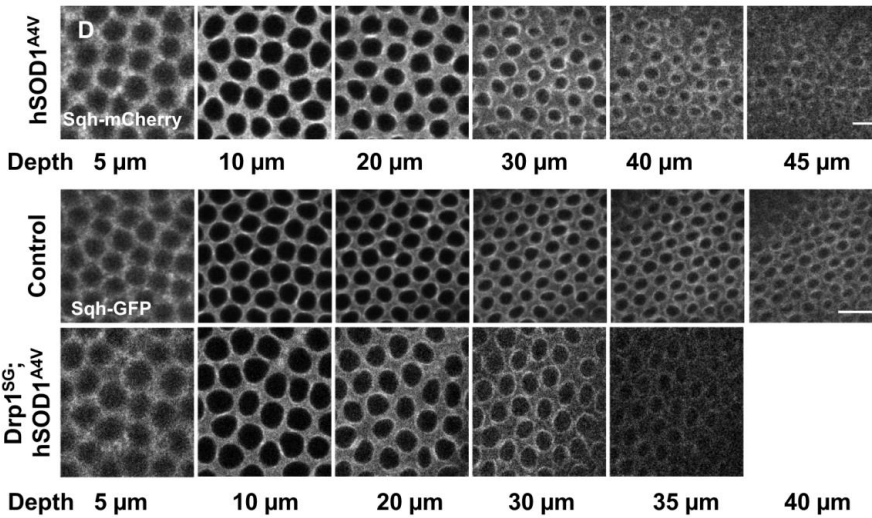
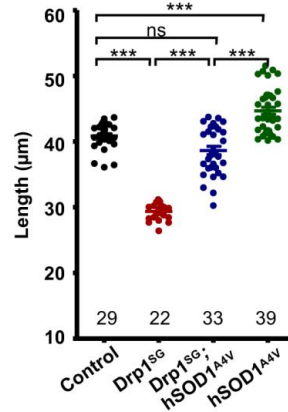
(blue) embryos is significantly smaller than Drp1^{SG} **(red)** embryos **(B)** indicating suppression of shape defect. The relative mitochondrial area at the apical regions in hSOD1^{A4V} **(green)** and Drp1^{SG}; hSOD1^{A4V} **(blue)** quantified in embryos with membrane length above 12 μm is comparable to control **(black)** and significantly higher than Drp1^{SG} **(red)** indicating that mitochondrial translocation occurs in Drp1^{SG}; hSOD1^{A4V} **(C)**. Each data point represents the number of embryos analysed, also shown by the numbers on the plot. Approximately 15000 optically resolvable mitochondrial spots were counted per embryo across around 40 cells per embryo **(B, C)**. ns; $P \geq 0.05$, *; $P \leq 0.05$, **; $P \leq 0.01$, ***; $P \leq 0.001$, Mann Whitney test) **(B, C)**. Scale bar: 5 μm **(A)**.



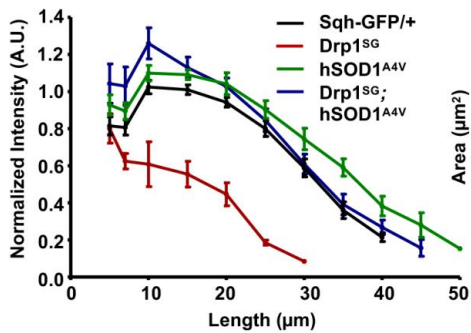
B Cellularization furrow progression



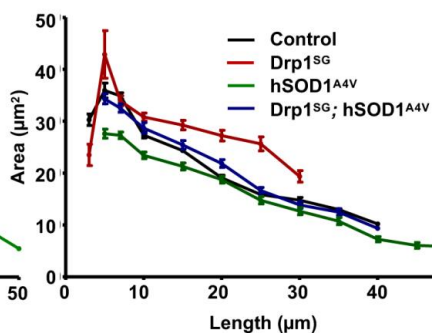
C Length at Cellularization end



E Sqh Intensity at contractile rings



F Area of Contractile rings



G Final Area of Contractile rings

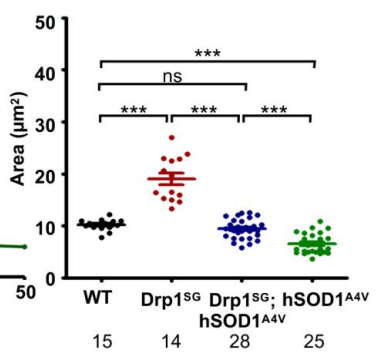


Figure 7: Contractile ring area and cell length defects in Drp1^{SG} are suppressed in Drp1^{SG}; hSOD1^{A4V} embryos.

(A-C) Cell length defects are suppressed in Drp1^{SG}; hSOD1^{A4V} embryos. hSOD1^{A4V} and Drp1^{SG}; hSOD1^{A4V} embryos are imaged sagittally using Sqh-mCherry and Sqh-GFP respectively (A). Membrane ingression, plotted with time during cellularization, is faster in hSOD1^{A4V} (green, B) and Drp1^{SG}; hSOD1^{A4V} (blue, B) compared to control (black, B, repeated from Figure 5B for comparison) embryos. Drp1^{SG}; hSOD1^{A4V} (blue, B) shows a suppression compared to Drp1^{SG} (red, B, repeated from Figure 5B). n = 4, 9 embryos for hSOD1^{A4V} and Drp1^{SG}; hSOD1^{A4V} respectively (B). Average final cell height achieved post cellularization (A, red arrowheads) in hSOD1^{A4V} (green, B, C) is significantly longer compared to control embryos (black, repeated from Figure 5C). Average final length in Drp1^{SG}; hSOD1^{A4V} embryos (blue, B, C) is suppressed as compared with Drp1^{SG} (red, repeated from Figure 5C) and is comparable with control (black, repeated from Figure 5C). n = 7, 8 embryos for hSOD1^{A4V} and Drp1^{SG}; hSOD1^{A4V} respectively (C). Number of furrows quantified are represented in the plot (C) (ns; P ≥ 0.05, ***, P ≤ 0.001, Mann Whitney test) (C). Scale bar: 5 μm (A)

(D-G) Sqh intensity at the contractile rings is suppressed in Drp1^{SG}; hSOD1^{A4V}. Sections through the furrow tips in Sqh-mCherry containing hSOD1^{A4V} and Sqh-GFP containing control and Drp1^{SG}; hSOD1^{A4V} embryos are shown (D). Mean Sqh-mCherry intensity in hSOD1^{A4V} (green, E) and Sqh-GFP intensity in Drp1^{SG}; hSOD1^{A4V} (blue, E) are quantified with respect to Sqh-mCherry (Figure 5E, black) and Sqh-GFP (Figure 6E, black) control embryos respectively. Mean Sqh-mCherry fluorescence intensity in hSOD1^{A4V} (green, E) is more than control Sqh-mCherry (Figure 5E, black). Mean Sqh-GFP intensity in Drp1^{SG}; hSOD1^{A4V} (blue, E) is comparable to control Sqh-GFP (black, E) and suppressed compared to Drp1^{SG} (red, repeated from Figure 5E). n = 6, 9 embryos for hSOD1^{A4V} and Drp1^{SG}; hSOD1^{A4V} respectively, 40 cells per embryo. Area of contractile rings quantified with respect to length shows increased constriction in hSOD1^{A4V} (green, F) compared to control (black, repeated from Figure 5F). Contractile ring area across membrane depth in Drp1^{SG}; hSOD1^{A4V} (blue, F) is comparable to control (black, repeated from Figure 5F) and is suppressed compared to Drp1^{SG} (red, repeated from Figure 5F). n = 6 embryos each for hSOD1^{A4V} and Drp1^{SG}; hSOD1^{A4V}, 5

rings each (**F**). Mean final ring area is significantly smaller in hSOD1^{A4V} (**green, G**) compared to control and Drp1^{SG} embryos (**black, red**, repeated from Figure 5G). Mean final area in Drp1^{SG}; hSOD1^{A4V} (**blue, G**) is comparable to control (**black**, repeated from Figure 5G) and is significantly smaller than Drp1^{SG} (**red**, repeated from Figure 5G) embryos. n = 6 embryos for hSOD1^{A4V} and Drp1^{SG}; hSOD1^{A4V}, number of contractile rings quantified are indicated in the plot (**G**). (ns; P ≥ 0.05, ***; P ≤ 0.001, Mann Whitney test) (**G**). Scale bar: 5 μm (**D**)

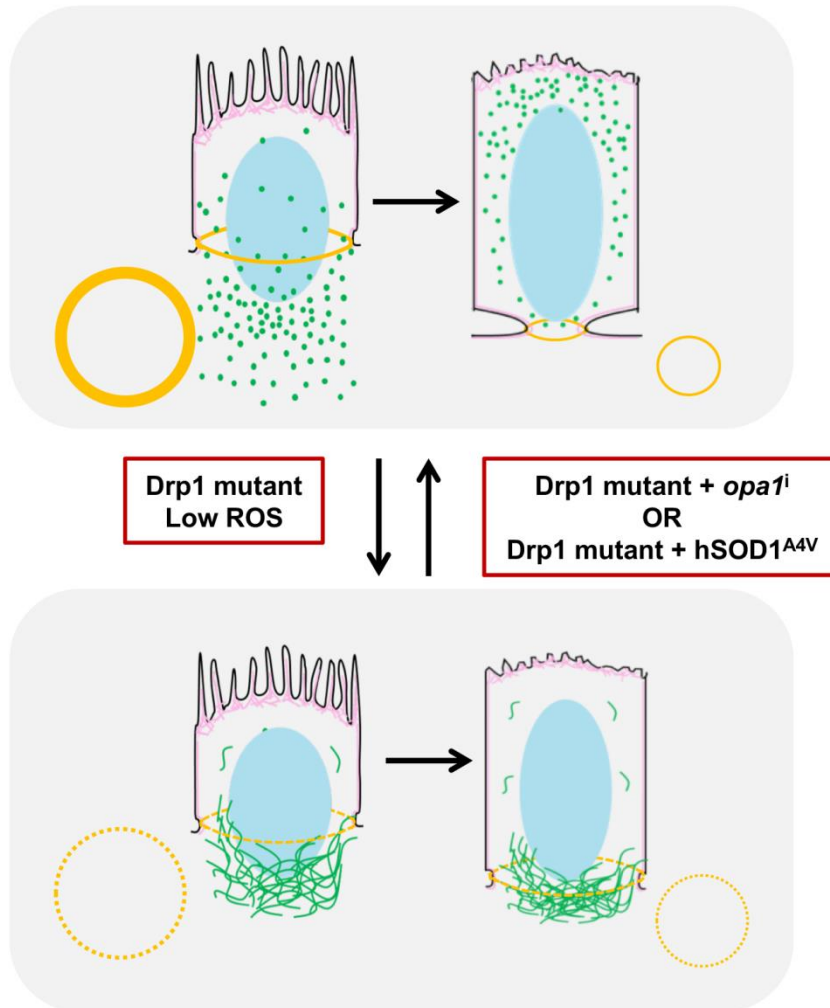


Figure 8: Summary

Mitochondria (green) translocate on microtubules towards apical regions synchronously with furrow ingression and ring constriction (Myosin, yellow) during cellularization. Clustered and presumably fused mitochondria (depicted as green filaments) in *drp1* mutants lead to low ROS and are not transported apically leading to defects in furrow ingression and ring constriction, due to loss of active Myosin II (dotted yellow) from the contractile rings. These defects are suppressed by either forced fragmentation of mitochondria using *opa1ⁱ* or by supplementing ROS by expressing hSOD1^{A4V} along with Drp1^{SG}. The data suggest that Myosin II activity during cellularization is regulated by optimal levels of ROS maintained by mitochondrial shape and/or localization.